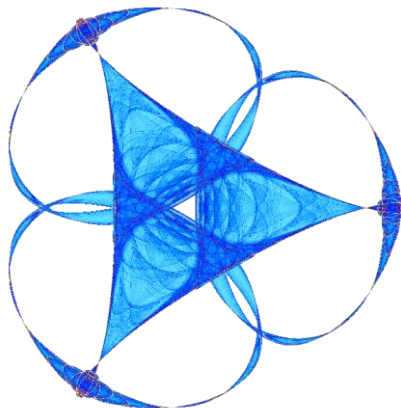# COMPUTED TEAR FILM AND OSMOLARITY DYNAMICS ON AN EYE-SHAPED DOMAIN

By

**Longfei Li, Richard J. Braun, Tobin A. Driscoll, William D. Henshaw,
Jeffrey W. Banks and P. Ewen King-Smith**

Computed Tear Film and Osmolarity Dynamics on an Eye-Shaped Domain

Longfei Li, Richard J. Braun* and Tobin. A. Driscoll

Department of Mathematical Sciences, University of Delaware, Newark, DE 19711, USA

*Corresponding author: braun@math.udel.edu

William D. Henshaw

Department of Mathematical Sciences, Rensselaer Polytechnic Institute, Troy, NY 12180, USA

Jeffrey W. Banks

Lawrence Livermore National Laboratory, Box 808, L-422, Livermore, CA 94551-0808, USA

AND

P. Ewen King-Smith

College of Optometry, The Ohio State University, Columbus, OH 43218, USA

[Last modified: July 29, 2014]

The concentration of ions, or osmolarity, in the tear film is a key variable in understanding dry eye symptoms and disease. In this manuscript, we derive a mathematical model that couples osmolarity (treated as a single solute) and fluid dynamics within the tear film on a 2D eye-shaped domain. The model includes the physical effects of evaporation, surface tension, viscosity, ocular surface wettability, osmolarity, osmosis and tear fluid supply and drainage. The governing system of coupled nonlinear PDEs is solved using the Overture computational framework, together with a new hybrid time-stepping scheme, using variable step BDF and RKC methods that were added to the framework. The results of our numerical simulations show good agreement with existing 1D models for both tear film and osmolarity dynamics and provide new insight about the osmolarity distribution over the ocular surface during the interblink.

Keywords: lubrication theory; osmolarity dynamics; tear film; thin film; composite overlapping grid.

1. Introduction

The purpose of the model we develop here is to compute the dynamics of fluid motion and osmolarity of the tear film on an eye-shaped domain. Osmolarity is the concentration of ions in solution. Given a 1M concentration of NaCl solution, each molecule of salt dissociates into two ions, and the osmolarity is then 2M. (Here M denotes molar concentration, which is moles per liter of solvent.) For a brief introduction to the mathematical models for the osmolarity and tear film dynamics, see the review by Braun (2012) or the paper by Zubkov et al. (2012).

The osmolarity is an important variable to include in tear film modeling because it is thought to be critical in the onset and subsequent development of dry eye syndrome (DES). A properly functioning tear film maintains a critical balance between tear secretion and loss within each blink cycle. Malfunction or deficiency of the tear film causes a collection of problems that are believed to comprise DES (Lemp, 2007). DES symptoms include, but are not limited to, blurred vision, burning, foreign body sen-

sation, tearing and inflammation of the ocular surface. Studies up to 2007 estimate that there are 4.91 million Americans suffering from DES (Anonymous, 2007). The ocular surface community is interested in understanding the function of the tear film (Johnson and Murphy, 2004) as well as the interaction of tear film dynamics and the connection between tear film volume, evaporation and break up with DES (Anonymous, 2007).

We summarize a discussion of the role of osmolarity on the ocular surface from Baudouin et al. (2013) here. According to Tietz (1995), in healthy blood the osmolarity is in the range 285-295 Osm/m^3 (also denoted mOsm/L or mOsM). In the healthy tear film, there is homeostasis with the blood in the range 296-302 Osm/m^3 (Lemp et al., 2011; Tomlinson et al., 2006; Versura et al., 2010). In DES, the lacrimal system is unable to maintain this homeostasis and osmolarity values in the meniscus rise to 316-360 Osm/m^3 (Tomlinson et al., 2006; Gilbard et al., 1978; Sullivan et al., 2010), and may rise to even higher values over the cornea. Using in vivo experiment and sensory feedback, Liu et al. (2009) estimated peak values of 800-900 Osm/m^3. Similar or higher values were computed from mathematical models of tear film break up in King-Smith et al. (2010) and Peng et al. (2014). We use a mathematical model to compute osmolarity over the entire exposed ocular surface subject to the assumptions stated in the Formulation section.

The method of tear sample collection and measurement is important. To our knowledge, osmolarity measurements in humans have been from samples in the inferior meniscus or the lower fornix. The lower fornix has a lower osmolarity than the meniscus (Mishima et al., 1971), and samples from the meniscus are most commonly used today. Gilbard et al. (1978) summarized the use of prior measurement techniques that used pipettes or capillary tubes to collect tear samples. Older methods may have used pipettes that took too large a sample compared to the tear film total volume, and could induce reflex tearing. In the exquisitely sensitive eye, this is a significant concern that could dilute or otherwise change the chemistry of the tear sample. Some capillary techniques are difficult to use, and the method of Gilbard et al. (1978) appeared to be easier to use; we note that the paper does not indicate where in the inferior meniscus the measurement was taken. Subsequent to sample collection, older techniques relied on freezing point depression to determine the osmolarity of the sample to about 1% error. More recently, a calibrated resistance measurement using the TearLab device allows rapid determination of osmolarity with an error for in vitro samples of about 1-2% error (Lemp et al., 2011; TearLab, 2013). In the approach, a sensor is touch to the meniscus at the temporal canthus, and the result is returned in less than a minute after the sample is taken. The latter approach is much more convenient for clinical use.

The level of effectiveness of osmolarity measurement to diagnose dry eye and to measure progression of the disease is still a matter of debate; for recent viewpoints, see for example Lemp et al. (2011); Amparo et al. (2013); Pepose et al. (2014); Amparo et al. (2014); Sullivan (2014). We found the summary by Baudouin et al. (2013) in their sections III and IV to be informative. We do not aim to settle the debate here, but to supply context for the measurements in the form of a quantitative prediction of the osmolarity over the entire exposed ocular surface to aid interpretation.

We now turn to previous work on the properties and dynamics of the tear film, relying heavily on the introduction from Li et al. (2014). Commonly, the tear film is described as a thin liquid film with multiple layers. At the anterior interface with air is an oily lipid layer that decreases the surface tension and retards evaporation, both of which help to retain a smooth well-functioning tear film (Norn, 1979). The aqueous layer is posterior to the lipid layer and consists mostly of water (Holly, 1973). At the ocular surface, there is a region with transmembrane mucins protruding from the cells in the corneal or conjunctival epithelia. This forest of glycosolated mucins, called the glycocalyx, has been referred to as the mucus layer in the past. It is generally agreed that the presence of the hydrophilic glycocalyx on the ocular surface prevents the tear film from dewetting (Bron et al., 2004; Gipson, 2004; Govindarajan and

Gipson, 2010). The overall thickness of the tear film is a few microns (King-Smith et al., 2004), while the average thickness of the lipid layer is on the order of 50 to 100nm (Norn, 1979; King-Smith et al., 2011) and the thickness of the glycocalyx is a few tenths of a micron (Govindarajan and Gipson, 2010). This structure is rapidly reformed, on the order of one second, after each blink in a properly-functioning tear film.

The aqueous part of tear fluid is supplied from the lacrimal gland near the temporal canthus and the excess is drained through the puncta near the nasal canthus. Mishima et al. (1966) estimated the total tear volume and the rate of influx from the lacrimal gland, as well as the time for the entire volume of tear fluid to be replaced (tear turnover rate); Zhu and Chauhan (2005) reviewed experiments on tear drainage and developed a mathematical model for drainage rates of the aqueous component through the puncta. Doane (1981) proposed the mechanism of tear drainage *in vivo* whereby tear fluid is drained into the canaliculi through the puncta during the opening interblink phase. The drainage stops when the pressure equalizes in the canaliculi. Water lost from the tear film due to evaporation into air is an important process as well (Mishima and Maurice, 1961; Tomlinson et al., 2009; Kimball et al., 2010). This is the primary mechanism by which the osmolarity is increased in the tear film.

The supply and drainage of tear fluid affects the distribution and flow of the tear film. A number of methods have been used to visualize and/or measure tear film thickness and flow, including interferometry (Doane, 1989; King-Smith et al., 2004, 2009), optical coherence tomography (Wang et al., 2003), fluorescence imaging (Harrison et al., 2008; King-Smith et al., 2013) and many others. We mention only a small number here that are relevant for our discussion of tear fluid flow over the exposed ocular surface. Maurice (1973) inserted lamp black into the tear film and watched their trajectories with a slit lamp. He observed that the particle paths in the upper meniscus near the temporal canthus diverge, with some particles proceeding toward the nasal canthus via the upper meniscus and others going around the outer canthus before proceeding toward the nasal canthus via the lower meniscus. (To our knowledge, no images from this experiment exist.) We use the term "hydraulic connectivity" as shorthand for this splitting of flow connecting the menisci. A similar pattern of the tear film was observed by Harrison et al. (2008) using fluorescein to visualize the tear film thickness. In this experiment, concentrated sodium fluorescein is instilled in the eye. Shining blue light on the eye causes the fluorescein to glow green; the fluorescence allows one to visualize the tear film (Lakowicz, 2006). The concentration is such that, if evaporation occurs, the concentration of fluorescein increases and the intensity of the fluorescence decreases; if fresh tear fluid enters the tear film, the concentration decreases and fluorescent intensity increases (Webber and Jones, 1986; Nichols et al., 2012; Braun et al., 2014). Harrison et al. (2008) visualized the entry of fresh tear fluid into the meniscus near the outer canthus, where the tear film was observed to brighten. Subsequently, this bright region split and fluid moved toward the nasal canthus along both the upper and lower lids via the menisci. The fluorescence could thus visualize hydraulic connectivity in the flow of tears. Similar experiments in King-Smith et al. (2013) and Li et al. (2014) visualized flow by using fluorescein instilled by drops in the tear film, and the mathematical model developed by Li et al. (2014) exhibited hydraulic connectivity in a very similar way to the experimental results shown in that paper.

The tear film is also redistributed near the eyelid margins by surface tension. The curvature generated by the meniscus creates a low pressure which draws in fluid from surrounding areas, creating locally thin regions near the meniscus. When fluorescein is used to visualize tear film thickness, this locally thin region near the lids is dark, and had been called the "black line." The black line is typically thought to be a barrier between the meniscus at the lid margins and the rest of the tear film (McDonald and Brubaker, 1971; Miller et al., 2002). Finally, though the healthy ocular surface is wettable, the tear film may still rupture; the term break up is used in the ocular science community for this phenomenon. The surface

tension of the tear/air interface, the wettability of the ocular surface, and the osmolarity are among the effects that we include in this study.

A variety of mathematical models have incorporated various important effects of tear film dynamics as recently reviewed by Braun (2012). The most common assumptions for these models are a Newtonian tear fluid and a flat cornea (Berger and Corrsin, 1974; Braun et al., 2012). Tear film models are often formulated on a one-dimensional (1D) domain oriented vertically through the center of the cornea with stationary ends corresponding to the eyelid margins. We refer to models on this kind of domain as 1D models. Surface tension, viscosity, gravity and evaporation are often incorporated into 1D models (Wong et al., 1996; Sharma et al., 1998; Miller et al., 2002; Braun and Fitt, 2003). Winter et al. (2010) improved previous evaporation models by including a conjoining pressure from van der Waals forces that approximated the wettable corneal surface. Incorporating heat transfer from the underlying eye, Li and Braun (2012) resolved a discrepancy of the tear film surface temperature between predictions of existing evaporation models and *in vivo* measurements.

Recently, studies of 1D models that bring together the interblink period and a moving end that represents the upper lid have appeared. Jones et al. (2005, 2006) developed models for tear film formation and relaxation that were unified in this way; one end of the domain moved to model the upper lid motion during the opening phase of the blink, then remained stationary for the subsequent relaxation during the interblink. Braun and King-Smith (2007) modeled eyelid motion for blink cycles by moving one end of the domain sinusoidally and they computed solutions for multiple complete blink cycles. Heryudono et al. (2007) followed their study with a more realistic lid motion and specified a flux boundary condition. Good agreement on tear film thickness between experiments and simulations was found by Heryudono et al. (2007). Deng et al. (2013, 2014) extended the model of Li and Braun (2012) to include upper lid motion (blink) and heat transfer from the underlying eye to explain observed ocular surface temperature measurements and to give new transient temperature results inside the eye. Bruna and Breward (2014) studied a model that added a dynamic lipid layer to an underlying aqueous layer with an insoluble surfactant at the lipid/aqueous interface (representing polar lipids). They computed dynamic results for the model and found various useful limits for it.

Braun (2012) gave a model for a spatially uniform film with no space dependence that was very similar to the one first suggested by King-Smith et al. (2007). The original model was a single ordinary differential equation for the tear film thickness that included evaporation from the tear/air interface at a constant rate and osmotic flow from the tear/cornea interface that was proportional to the osmolarity increase above the isotonic value. The latter assumption simplifies the tear/cornea interface to a semi-permeable boundary that allows water but not solutes to pass. They found that the model predicted equilibration of the tear film thickness at values greater than the height of the glycocalyx for sufficiently large permeability of the tear/cornea interface. They also found that the osmolarity could become quite large as the tear film thinned for small permeability values, as much as 10 times the isotonic value under some conditions. The model given in Braun (2012) included van der Waals forces that stopped thinning at the purported height of the glycocalix which allowed the model to be used at zero permeability at the tear/cornea interface. Similar conclusions about the osmolarity during thinning were found there.

These models were extended to include a specified evaporation profile that varied in space by King-Smith and coworkers (King-Smith et al., 2010). The evaporation profile was Gaussian with a peak value that could be specified larger than the surrounding constant rate. The local thinning caused by locally increased evaporation led to increased osmolarity in the break up region, which could be several times larger than the isotonic value. A modified evaporation distribution was created by Peng et al. (2014) that had two parts. One part used an immobile lipid layer with specified thickness and fixed resistance to diffusion through it by water. The other part was a resistance to transport in the air outside the tear

film; this second resistance included convective and diffusive transport in the air. They also found that the osmolarity was elevated in this model for break up.

Zubkov et al. (2012) developed a model describing the spatial distribution of tear film osmolarity that incorporates both fluid and solute (osmolarity) dynamics, evaporation, blinking and vertical saccadic eyelid motion. They found that both osmolarity was increased in the black line region and that measurements of the solute concentrations within the lower meniscus need not reflect those elsewhere in the tear film. This model gave results over a line oriented vertically through the center of the cornea, and thus gave information about the osmolarity over more of the ocular surface than the models mentioned above.

In this paper, we study dynamics of the fluid motion and osmolarity on an eye-shaped domain. To our knowledge, Maki, Braun, Henshaw and King-Smith (2010); Maki, Braun, Ucciferro, Henshaw and King-Smith (2010) were the first to extend models of fluid dynamics in the tear film to a geometry that approximated the exposed ocular surface. They formulated a relaxation model on a stationary 2D eye-shaped domain that was approximated from a digital photo of an eye. They specified tear film thickness and pressure boundary conditions (Maki, Braun, Henshaw and King-Smith, 2010) or flux boundary conditions (Maki, Braun, Ucciferro, Henshaw and King-Smith, 2010). Their simulations recovered features seen in 1D models such as formation of the black line, and captured some experimental observations of the tear film dynamics around the lid margins. Maki, Braun, Ucciferro, Henshaw and King-Smith (2010) simplified the *in vivo* mechanisms and imposed a flux boundary condition having only spatial dependence (specifying the location of the lacrimal gland and the puncta holes) in their tear film relaxation model. Under some conditions, they were able to recover hydraulic connectivity as seen experimentally and described above. Li et al. (2014) improved the model, added evaporation and a wettable ocular surface, as well as a time-dependent boundary condition that approximated the in- and out-flow of the aqueous layer of the tear film.

In this paper, we formulate a tear film dynamics model on a 2D eye-shaped domain that incorporates osmolarity transport and osmosis from the tear/eye interface. The permeability of the ocular surface will be either constant over the whole surface, or a space-dependent function with lower permeability over the cornea and higher permeability over the conjunctiva. The model will lose water via evaporation to the air, gain water from the ocular surface, and, via the flux boundary condition, will have water supplied as from the lacrimal gland and removed as from the puncta. The model captures the previous fluid dynamics results achieved before, such as hydraulic connectivity, and adds significant new results about the distribution of osmolarity over the exposed ocular surface. We believe that these results will impact the understanding of osmolarity dynamics in the tear film as well as the measurement of this important quantity.

We begin by formulating the model in Section §2. A brief description of the numerical methods used for the simulation is discussed in Section §3, followed by detailed results of simulations and comparison with experiments in Section §4. Conclusions and further directions are pointed out in Section §5.

2. Formulation

In this section, we present a mathematical model that incorporates osmolarity and fluid dynamics into a tear film model on a 2D eye shaped domain as shown in Figure 1. In Figure 1, (u', v', w') are the velocity components in the coordinate directions (x', y', z'); z' is directed out of the page and primed variables are dimensional. g' is gravity which is specified in the negative y' direction.

The boundary curves of the eye-shaped domain are approximated from a digital photo by four polynomials. Two are parabolas in x' and two are ninth-degree polynomials in y', and C_4 continuity is

imposed where they join (indicated by dots) (Maki, Braun, Henshaw and King-Smith, 2010; Maki, Braun, Ucciferro, Henshaw and King-Smith, 2010; Li et al., 2014). s' is the arc length of the boundary starting at the joint of the nasal canthus and upper lid, and is traversed in the counterclockwise direction as s' increases. The unit vectors tangential and normal to the boundary curves are given by $\mathbf{t}'_b$ and $\mathbf{n}'_b$, respectively. $z' = h'(x', y', t')$ denotes the free surface of tear film and t' is the time.
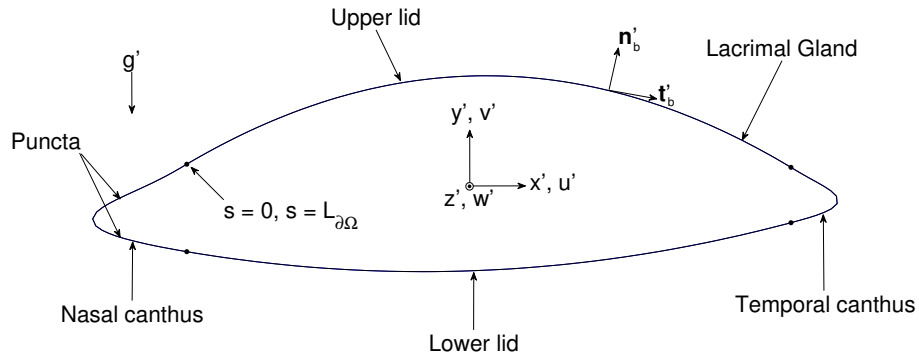

FIG. 1: The coordinate system and eye-shaped domain. The z' direction points out of the page.

We assume that the tear fluid is incompressible and Newtonian with constant density ρ, viscosity μ, specific heat c_p, and thermal conductivity k. We also assume the ocular surface is flat due to the fact that the characteristic thickness of the human tear film is much less than the radius of curvature of the ocular globe (Berger and Corrsin, 1974; Braun et al., 2012). The governing equations for the tear film thickness $h'(x', y', t')$ and the osmolarity $c'(x', y', t')$ are derived from the incompressible Navier-Stokes and convection-diffusion equations, respectively. The two equations are coupled by the osmotic flux, that is, the fluid that flows from the ocular surface at $z' = 0$ into the tear film driven by the osmolarity difference between the tear film and the cornea (Levin and Verkman, 2004). In the model, water is lost to the air, treated as a passive gas outside the tear film ($z' > h'$), and water is supplied due to the subsequent increased osmolarity via this osmotic flux.

After nondimensionalization and simplification using lubrication theory (e.g. Jensen and Grotberg (1993); Braun (2012)), we arrive at a system of PDEs for the dimensionless variables $h(x, y, t)$ and $c(x, y, t)$:

$$\partial_t h + EJ + \nabla \cdot \mathbf{Q} - P_c(c - 1) = 0, \tag{2.1}$$

$$h\partial_t c + \nabla c \cdot \mathbf{Q} = EcJ + \frac{1}{\mathrm{Pe}_c}\nabla \cdot (h\nabla c) - P_c(c - 1)c. \tag{2.2}$$

The evaporative mass flux J is given by

$$J = \frac{1 - \delta\left(S\Delta h + Ah^{-3}\right)}{\bar{K} + h},$$

and the fluid flux $\mathbf{Q}$ across any cross-section of the film is given by

$$\mathbf{Q} = \frac{h^3}{12}\nabla\left(S\Delta h + Ah^{-3} - Gy\right).$$

The nondimensional parameters that arise are defined and given values in the following section and in Table 1. The dimensional parameters used in those expression are given in Table 2. A detailed derivation of the governing equations (2.1) and (2.2) can be found in Appendix A.

2.1 *Parameter Descriptions*

Lubrication theory exploits the small value of ε, which is the ratio of the tear film thickness to the length scale along the tear film. E characterizes the evaporative contribution to the surface motion, δ measures the pressure influence to evaporation, S is the ratio of surface tension to viscous forces, A is the Hamaker constant in nondimensional form related to the unretarded van der Waals force, G is the ratio of gravity to the viscous force, $\bar{K}$ represents the non-equilibrium parameter that sets the evaporative mass flux, Pe_c is the Péclet number for the osmolarity describing the competition between convection and diffusion, and P_c is the water permeability of the ocular surface (P_{corn} and P_{conj} specify the values of P_c over the cornea and conjunctiva, respectively).

Evaporation makes major contributions to tear film thinning between blinks (Kimball et al. (2010) and references therein) and increases the osmolarity of tears, which in turn induces an osmotic flow through the ocular surface that compensates for much of the evaporative water loss. Nichols et al. (2005) have found that the mean rate of thinning of the pre-cornea tear film is $3.79 \pm 4.20\mu$m/min, and the histogram of their measurements shows an asymmetrical distribution, with narrow peaks corresponding to a thinning rate of approximately 1 μm/min but with many instances of much more rapid thinning. Based on these experimental measurements, we tune the non-equilibrium parameter $\bar{K}$ that sets the evaporative mass flux such that the thinning rate of flat tear film (i.e. neglecting all the spatial derivatives) is 4μm/min. The model does not take into account transport or the relative humidity outside the tear film as in Peng et al. (2014); it is suitable for controlled laboratory conditions.

2.2 *Permeability of the ocular surface*

The ocular surface is believed to be permeable, and the induced osmotic flow helps to arrest tear film thinning and hence ameliorate osmolarity elevation (Braun, 2012). In addition, the water permeability over the ocular surface is not a constant; the conjunctiva is normally more permeable than the cornea Dartt (2002). King-Smith and coworkers proposed values for the water permeability of the ocular surface, that is, 12.0μm/s for the cornea and 55.4μm/s for the conjunctiva (King-Smith et al., 2010; Bruhns et al., 2014). We use these values to determine the dimensionless permeability P_c in the model as follows: we first define the corneal region as a unit circle with the center $\mathbf{X_c} = (0.05, 0.225)$ in the domain shown in Figure 1, and the variable permeability at any position $\mathbf{X} = (x, y)$ is then defined as

$$P_c(x,y) = \frac{P_{\mathrm{conj}} - P_{\mathrm{corn}}}{2}\tanh\left(\frac{|\mathbf{X} - \mathbf{X_c}| - 1}{0.05}\right) + \frac{P_{\mathrm{conj}} + P_{\mathrm{corn}}}{2}. \tag{2.3}$$

Here $P_{\mathrm{conj}} = 0.06$ is the dimensionless permeability of conjunctiva , $P_{\mathrm{corn}} = 0.013$ is the dimensionless permeability of cornea, and $|\mathbf{X} - \mathbf{X_c}|$ is the distance between points $\mathbf{X}$ and $\mathbf{X_c}$. Figure 2 plots the distribution of the variable permeability on the eye-shaped domain.

Parameter	Expression	Value
ε	$\dfrac{d'}{L'}$	1×10^{-3}
E	$\dfrac{k(T'_B - T'_s)}{d'\mathscr{L}_m \varepsilon \rho U_0}$	118.3
S	$\dfrac{\sigma \varepsilon^3}{\mu U_0}$	6.92×10^{-6}
$\bar{K}$	$\dfrac{kK}{d'\mathscr{L}_m}$	8.9×10^3
G	$\dfrac{\rho g (d')^2}{\mu U_0}$	0.05
δ	$\dfrac{\alpha \mu U_0}{\varepsilon^2 L'(T'_B - T'_s)}$	4.66
A	$\dfrac{A^*}{L'd\mu U_0}$	2.14×10^{-6}
Pe_c	$\dfrac{U_0 L'}{D_c}$	9.62×10^3
P_{corn}	$\dfrac{P_{\text{corn}}^{\text{tiss}} v_w c_0}{\varepsilon U_0}$	0.013
P_{conj}	$\dfrac{P_{\text{conj}}^{\text{tiss}} v_w c_0}{\varepsilon U_0}$	0.06

Table 1: Dimensionless Parameters. Values and descriptions of the dimensional parameters appeared are given in Table 2.

2.3 *Boundary conditions*

Along the boundary of the eye-shaped domain (denoted as $\partial \Omega$), we prescribe the constant tear film thickness

$$h|_{\partial \Omega} = h_0. \tag{2.4}$$

We set $h_0 = 13$ in the computation because this choice is in the range of experimental measurement (48 – 66μm or 9.6 – 13.2 nondimensionally) from Golding et al. (1997). In addition, we specify the normal component of the fluid flux,

$$\mathbf{Q} \cdot \mathbf{n}_b = Q_{lg}(s,t) + Q_p(s,t), \tag{2.5}$$

according to the mechanism of Doane (1981) for tear supply and drainage, and the tear drainage model of Zhu and Chauhan (2005), but with simplification regarding blinking. This fluid flux boundary condition mimics some effects of blinking by providing a time-dependent influx through the lacrimal gland and efflux through the puncta. Specifically, the lacrimal gland supply is specified as on at the beginning

Parameter	Description	Value	Reference
μ	Viscosity	1.3×10^{-3}Pa·s	Tiffany (1991)
σ	Surface tension	0.045N·m^{-1}	Nagyová and Tiffany (1999)
k	Tear film thermal conductivity	0.68W·m^{-1}·K^{-1}	Water
ρ	Density	10^3kg·m^{-3}	Water
$\mathscr{L}_m$	Latent heat of vaporization	2.3×10^6J·kg^{-1}	Water
T_s'	Saturation temperature	$27°$C	Estimated
T_B'	Body temperature	$37°$C	Estimated
g	Gravitational acceleration	9.81m·s^{-2}	Estimated
A^*	Hamaker constant	3.5×10^{-19}Pa·m^3	Winter et al. (2010)
α	Pressure coefficient for evaporation	3.6×10^{-2}K·Pa^{-1}	Winter et al. (2010)
K	Non-equilibrium coefficient	1.5×10^5K·m^2·s·kg^{-1}	Estimated
d'	Characteristic thickness	5×10^{-6}m	King-Smith et al. (2004)
L'	Half-width of palpebral fissure	5×10^{-3}m	Estimated
U_0	Characteristic speed	5×10^{-3}m/s	King-Smith et al. (2009)
$P_{\text{corn}}^{\text{tiss}}$	Tissue permeability of cornea	12.0μm/s	King-Smith et al. (2010)
$P_{\text{conj}}^{\text{tiss}}$	Tissue permeability of conjunctiva	55.4μm/s	King-Smith et al. (2010)
v_w	Molar volume of water	1.8×10^{-5}m^3·mol^{-1}	Water
D_c	Diffusivity of osmolarity in water	2.6×10^{-9}m^2/s	Zubkov et al. (2012)

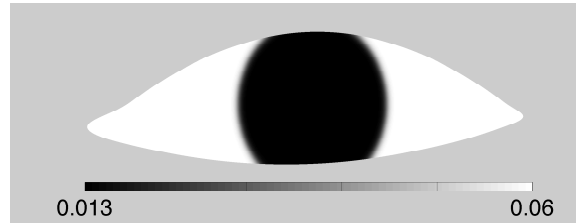Table 2: Dimensional Parameters.

FIG. 2: Variable permeability distribution over the ocular surface.

of a flux cycle, and the punctal drainage follows one time unit later. Both the supply and drainage start to shut off at t = 5. The duration of a complete flux cycle in the model is $\Delta t_{bc} = 10$. In Figure 3, we show a sequence of images of the fluid flux boundary condition (2.5) within a flux cycle. At $t = 0$ (Figure 3a), there is zero fluid flux on the boundary. At $t = 0.5$, we see the lacrimal gland supply is fully on while the drainage does not yet start in Figure 3b; the drainage begins at $t = 1$. In Figure 3c, both supply at the lacrimal gland and drainage at the two puncta holes remain fully on. Then, the fluid flux turns off at $t = 5$ and remains zero until the end of a flux cycle (t=10) as shown in Figure 3d. The influx and efflux are balanced in each flux cycle. See Appendix B and Li et al. (2014) for the detailed formula and a supplementary movie for the time-dependent flux boundary condition (2.5).

For the osmolarity $c(x,y,t)$, we consider two boundary conditions in this paper. Case (i) is the Dirichlet boundary condition

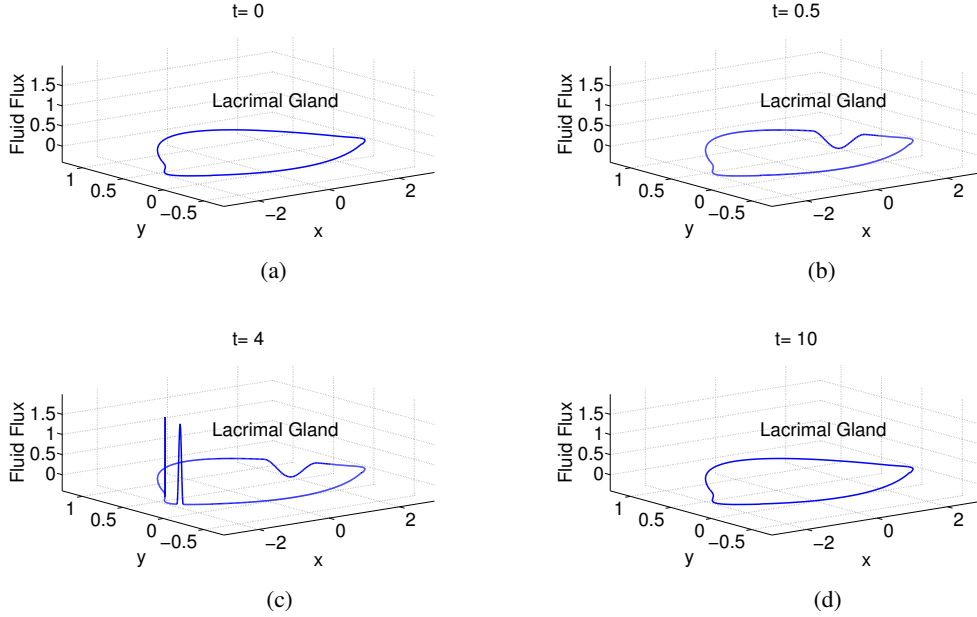$$c|_{\partial\Omega} = 1; \tag{2.6}$$

FIG. 3: Time sequences of fluid flux boundary condition during one flux cycle.

case (ii) is the homogeneous Neumann boundary condition

$$\nabla c \cdot \mathbf{n}_b|_{\partial\Omega} = 0. \tag{2.7}$$
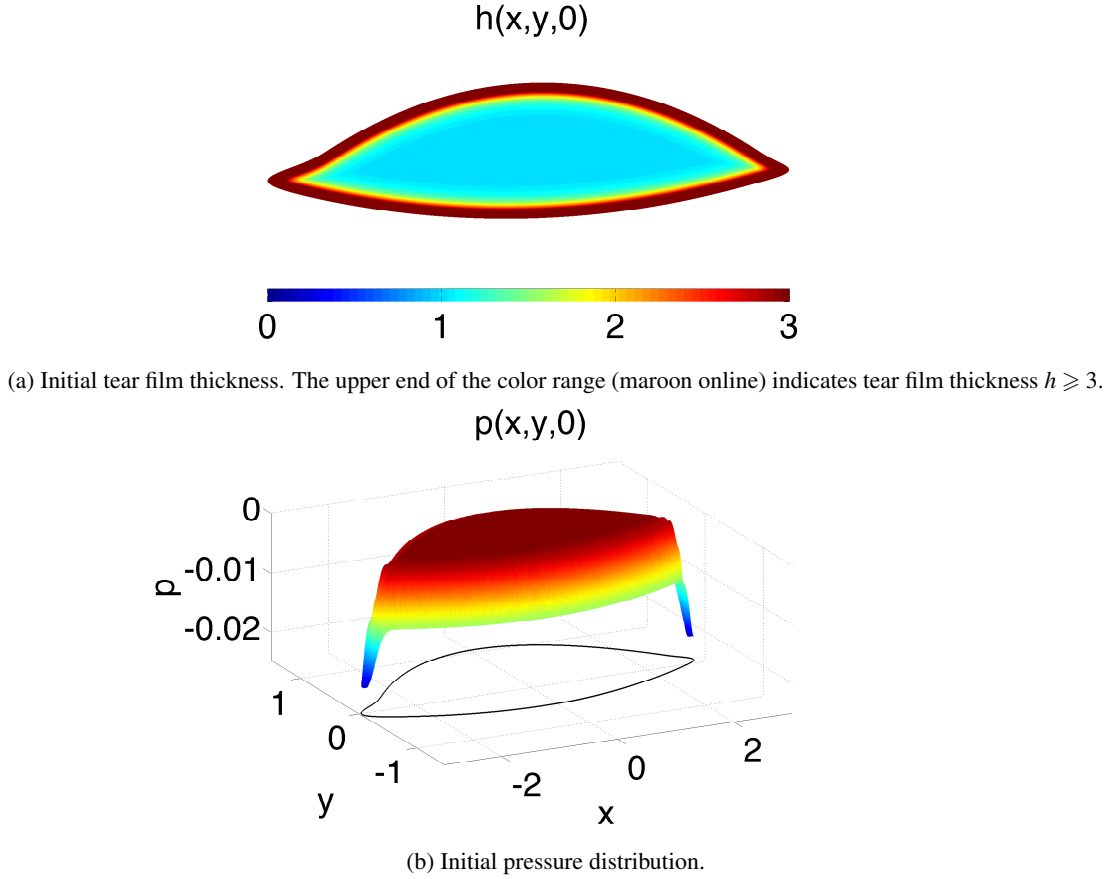
2.4 *Initial Condition*

The initial condition $h(x,y,0)$ is specified based on a numerically smoothed version of the function

$$h(x,y,0) = 1 + (h_0 - 1)e^{-\min(\text{dist}((x,y),\partial\Omega))/x_0}, \tag{2.8}$$

where $x_0 = 0.06$ and $\text{dist}(\mathbf{X},\partial\Omega)$ is the distance between a point with position vector $\mathbf{X}$ and a point on the boundary $\partial\Omega$ (Maki, Braun, Henshaw and King-Smith, 2010; Maki, Braun, Ucciferro, Henshaw and King-Smith, 2010). It specifies a dimensional initial volume of about 1.805μl. This value is well within the experimental measurements by Mathers and Daley (1996), who found the volume of exposed tear fluid to be $2.23 \pm 2.5\mu$l. The initial pressure $p(x,y,0)$ is calculated from equation (3.2) accordingly (Li et al., 2014). Figure 4 shows the initial thickness h and pressure p that are implemented in the numerical simulations. For the initial osmolarity, we assume the salt-ions are well mixed and of the isosmotic physiological salt concentration (302 Osm/m^3, or 1 dimensionlessly) at the beginning, thereby specifying

$$c(x,y,0) = 1. \tag{2.9}$$

h(x,y,0)

(a) Initial tear film thickness. The upper end of the color range (maroon online) indicates tear film thickness $h \geqslant 3$.

p(x,y,0)

(b) Initial pressure distribution.

FIG. 4: Smoothed initial conditions for h and p.

3. Numerical Methods

For numerical purposes, we rewrite the model equations by introducing the pressure $p(x,y,t)$ as a new dependent variable:

$$\partial_t h + E\frac{1+\delta p}{\bar{K}+h} + \nabla \cdot \left[-\frac{h^3}{12}\nabla(p+Gy)\right] - P_c(c-1) = 0, \tag{3.1}$$

$$p + S\Delta h + Ah^{-3} = 0, \tag{3.2}$$

$$h\partial_t c + \nabla c \cdot \left[-\frac{h^3}{12}\nabla(p+Gy)\right] = Ec\frac{1+\delta p}{\bar{K}+h} + \frac{1}{\text{Pe}_c}\nabla \cdot (h\nabla c) - P_c(c-1)c. \tag{3.3}$$

The corresponding boundary conditions must be applied: (2.4), (2.5) and one of (2.6) or (2.7). Note that the flux condition (2.5) is readily converted into a Neumann condition on p. The initial conditions must be applied as well, using smoothed versions of (2.8) and (3.2), as well as (2.9)

We solve the equations (3.1)–(3.3) on the eye-shaped geometry (Figure 1) using the Overture computational framework (http://www.overtureframework.org. Primary developer and contact: W. D. Henshaw, henshw@rpi.edu), which is a collection of C++ libraries for solving PDEs on complex domains (Chesshire and Henshaw, 1990; Henshaw, 2002).
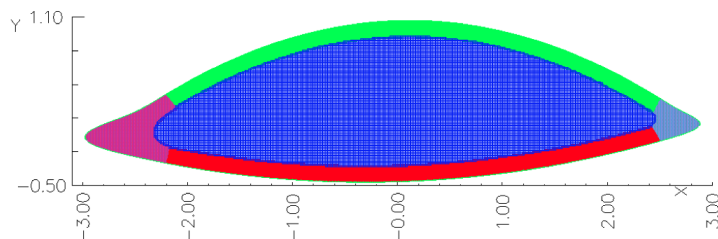
3.1 *Computational Grid*

FIG. 5: Computational grid on the eye-shaped domain.

The tear film is relatively thin and flat in most of the interior of the exposed ocular surface; the thickness increases rapidly near the eyelids forming relatively steep menisci around the boundary of corresponding computational domain. In order to solve the tear film model efficiently, we use five component grids, whose union is the computational grid. The component grids are one cartesian background grid that has grid lines aligned with the coordinate axes, and four boundary-fitted grids near the boundary. The solution values are interpolated between grids where they overlap. We generated a new computational grid using the grid generation capabilities of the Overture computational framework. We extend the boundary fitting grids from the boundary using transfinite interpolation (TFI), which is a generalized shearing transformation that maps the unit square onto the region bounded by four curves (Chesshire and Henshaw, 1990; Henshaw, 2002). Unlike grids based on extending normals from the boundary, we can extend the boundary-fitting grids as much as we want without worrying about intersecting normal lines. This provides us with the boundary-fitting grids that are wide enough to cover the menisci of the tear film. In addition, we double the grid spacing for the background Cartesian grid to reduce the number of grid points compared to previous work (Maki, Braun, Henshaw and King-Smith, 2010; Maki, Braun, Ucciferro, Henshaw and King-Smith, 2010; Li et al., 2014). The new grid, plotted in Figure 5, reduces the total number of grid points by about 14% while achieving better overall accuracy for test problems (the new grid has a total number of 235,018 grid points). Unless otherwise noted, all the simulation results presented in this paper are computed using the computational grid in Figure 5.

3.2   *A Hybrid Time-Stepping Scheme*

To solve the equations (3.1)–(3.3), we first discretize the spatial derivatives using the second-order accurate finite difference method for curvilinear and Cartesian grids from Overture. Since the model equations (3.1)–(3.3) are weakly coupled by osmosis (terms involving P_c), we developed a hybrid time stepping scheme to solve the coupled system: we first solve the equation (3.3) for c using a dynamic explicit Runge-Kutta-Chebyshev (RKC) method (Sommeijer et al., 1997); then we update the h and p equations (3.1) & (3.2) and solve them using the variable step size BDF method with fixed leading coefficient based on Brenan et al. (1996) and Maki, Braun, Henshaw and King-Smith (2010); Maki, Braun, Ucciferro, Henshaw and King-Smith (2010). The resulting nonlinear system of the BDF method is solved using Newton's iteration method. Solutions on different component grids are coupled by interpolation. The RKC method is suitable for this problem because it has an extended stability region with a stability bound that is quadratic in the number of stages, and the explicit method is fast and easy to implement. We exploit the nonlinear power method for an estimation of the largest eigenvalue of the spatially discretized system from (3.3) for c, and we use the quadratic relation to determine the number of stages needed for the RKC method. We have empirical criteria to determine whether an approximation is accepted or not. The number of stages is updated at every successful time step. More detailed results regarding the numerical analysis and performance of this method will appear elsewhere, since our focus is on the tear film here.

4. Results

In this section, we present computed results for the tear film thickness $h(x,y,t)$ and the osmolarity $c(x,y,t)$ on the 2D eye-shaped domain. We vary the water permeability P_c and the thinning rate (evaporation) that sets the non-equilibrium parameter $\bar{K}$ to study their influence on the dynamics of both tear film and osmolarity. We also explore two types of boundary condition for the osmolarity $c(x,y,t)$: (i) Dirichlet, given by (2.6), and (ii) homogeneous Neumann, given by (2.7).

4.1   *Constant Nonzero Permeability*

We begin by presenting results for the model with the same constant water permeability over the whole ocular surface; we use the corneal permeability corresponding to $P_c = 0.013$ measured by King-Smith et al. (2010); Bruhns et al. (2014). Figure 6 shows the contours of the simulation results. The left column represents the tear film thickness, and the right column represents the osmolarity. We see the dark band (blue online) set inside of the boundary, representing the so-called black line, emerges rapidly near to and inside of the menisci in the left column. The black line develops due to capillary action resulting from the positive curvature of the menisci generating a low pressure that sucks fluid into the meniscus. A local minimum thus forms near the meniscus, and is referred to as the black line. In addition, the canthi in the 2D eye-shaped domain induce a second direction of curvature, creating an even lower pressure that attracts fluid toward themselves. Therefore, the tear film near the two canthi is often thinner than other parts of the black line. In this case, the global minimum is located near the nasal canthus, which is sharper (more curved) than the temporal canthus. The formation of the global minimum is also promoted by the efflux of fluid near the nasal canthus due to the boundary conditions that mimic punctal drainage from this region. This also shows that both the thickness and osmolarity vary significantly away from the vertical line through the center of the cornea. Note 1D models formulated along this line do not account for this variation. The redistribution of fluid due to
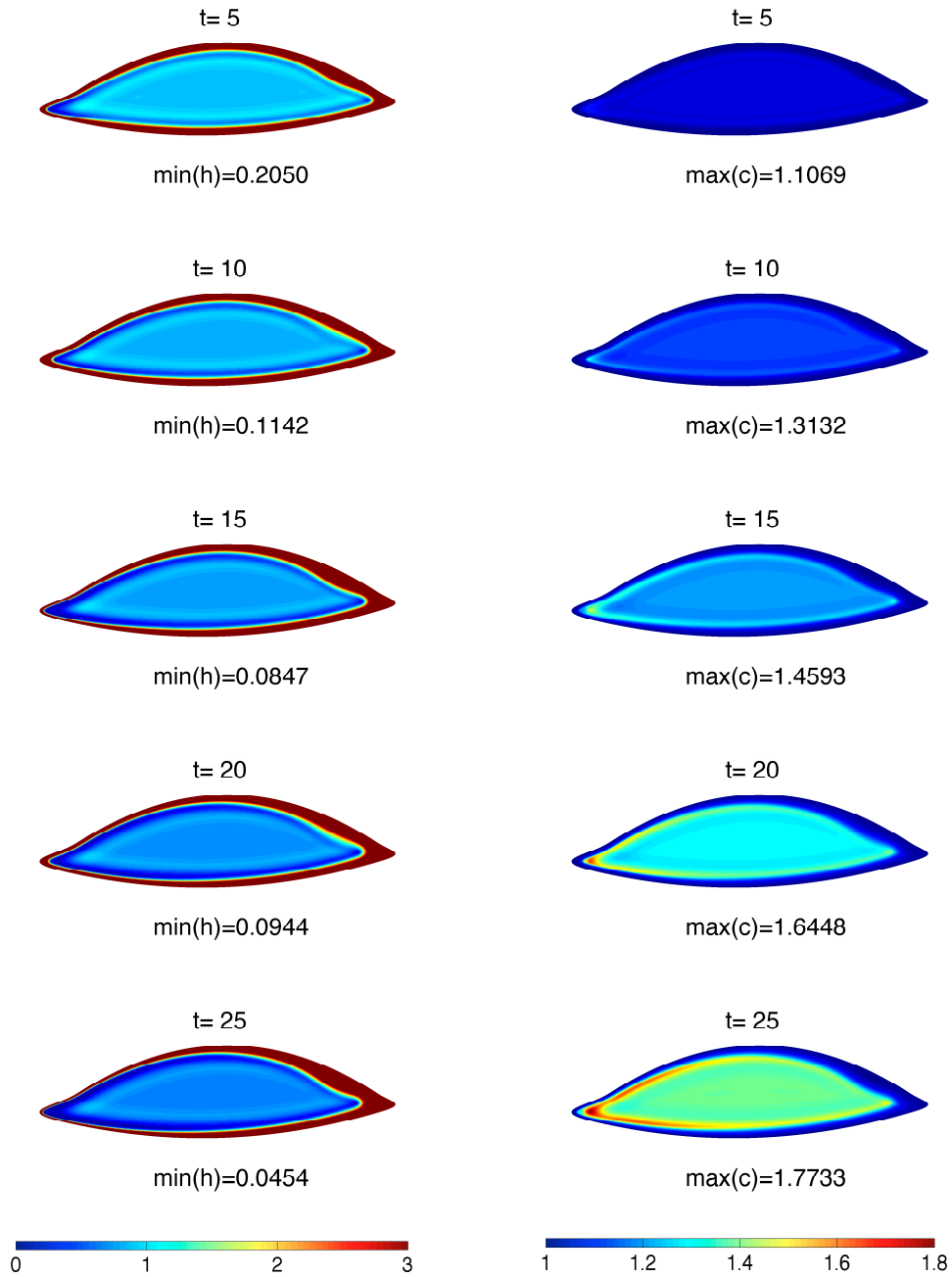
FIG. 6: Contours of tear film thickness (left column) and osmolarity (right column) with constant permeability of $P_c = 0.013$ all over the exposed ocular surface and with Dirichlet boundary condition (2.6) on the osmolarity. The thinning rate is 4μm/min.

surface tension also causes a small ridge to form on the interior side of the black line. This is seen as a light band (turquoise online) in the left column of Figure 6. This light band is a ridge that has been seen in a number of other studies (Maki, Braun, Henshaw and King-Smith, 2010; Maki, Braun, Ucciferro, Henshaw and King-Smith, 2010; Li et al., 2014). The tear film thickness in the interior decreases steadily throughout the computation because of evaporation; this is visualized by the continual darkening of the interior in the contour plots.

The corresponding osmolarity contours are plotted in the right column of Figure 6. Generally, the osmolarity increases more where the tear film is thinner, such as in the black line and canthi regions. This is in qualitative agreement with the results of Zubkov et al. (2012); we return to a direct comparison with their 1D results for $P_c = 0$ in the next section. The global maximum of osmolarity is in the nasal canthus that corresponds to the location of thinnest tear film. In the osmolarity plots, we observe a bright band indicating that a region of elevated osmolarity is forming near the developing black line. Osmolarity in the interior continues to increase as a result of evaporation, and the interior of the eye-shaped domain becomes brighter in the plots. In the region where tear film forms a small ridge, a corresponding darker band is also present on the interior side of the brighter band in the osmolarity plots.

The vertical cross-sectional plots ($x = 0$), shown in Figure 7, illustrate more directly the correlation between the tear film thickness and osmolarity: the osmolarity is roughly the reciprocal of the tear film thickness except in the black line and meniscus regions. Furthermore, comparison between Figure 7 and Figure 9 for the zero permeability case in the next section also reveals the effects of osmosis: the tear film is slightly thicker while the osmolarity is obviously smaller for the constant nonzero permeability case.
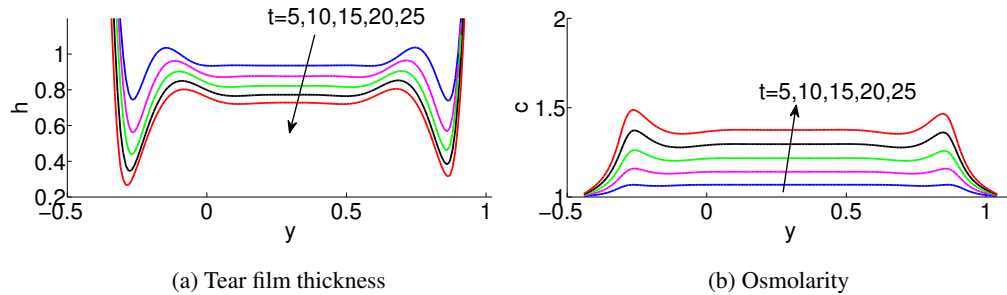

(a) Tear film thickness   (b) Osmolarity

FIG. 7: Cross-sectional plots through the vertical line $x = 0$ with $P_c = 0.013$ and Dirichlet boundary condition (2.6). The thinning rate is 4μm/min and the upper eyelid is located on the positive side of the y-axis.

4.2 *Zero Permeability*

Now, we consider our model on an impermeable ocular surface, i.e. $Pc = 0$, so as to reveal the effect of osmosis by comparing with the previous results in §4.1, and we make comparisons with existing studies on 1D domains to show that our model provides consistent predictions. In this case, no water is supplied in response to the increased osmolarity that occurs when water evaporates from the tear film. Figure 8 shows the contours of both tear film thickness and osmolarity on the eye-shaped domain at $t = 25$. It shows that both the thickness and osmolarity vary significantly away from the vertical line through the

center of the cornea. For example, the global minimum of tear film thickness is located in the nasal canthus and is much smaller than that in the cross-sectional plot. Furthermore, there is a spike in the osmolarity contour with a global maximum as large as $\max(c) = 4.8031$ in the nasal canthus. These global extrema and their locations can't be found via 1D models, and to our knowledge are not available from clinical measurements either. From Figure 8, we also see more elevated osmolarity at the black line region, and the lowest concentration is located near the lacrimal gland as a result of the fresh tear supply. The tear film dynamics predicted by this model are in agreement with previous results (Li et al., 2014).

The effect of osmosis can be readily seen by comparing the extreme values of different permeability cases. The extreme values of both h and c for several cases we considered in this paper are listed in Table 3. For the constant nonzero permeability case ($P_c = 0.013$), the minimum thickness ($\min(h) = 0.0454$) is slightly larger than that with zero permeability ($\min(h) = 0.0343$) at $t = 25$. However, the peak of osmolarity is significantly reduced by osmotic flows: $\max(c) = 1.7733$ with constant permeability and $\max(c) = 4.8031$ with zero permeability at $t = 25$. Therefore, according to our computation, we conclude that the presence of osmotic flux across the corneal surface may protect the tear film from excessive hyperosmolarity which could cause damage to the ocular surface and/or denaturation of tear film mucins and proteins (Govindarajan and Gipson, 2010).

	Thinning rate:	4 μm/min		10 μm/min	20 μm/min
	$P_c = 0$	$P_c = 0.013$	$P_c(x,y)$	$P_c(x,y)$	$P_c(x,y)$
$\min(h(x,y,5))$	0.2043	0.2050	0.2070	0.1880	0.1557
$\min(h(x,y,10))$	0.1072	0.1142	0.1294	0.1102	0.0931
$\min(h(x,y,15))$	0.0819	0.0847	0.0899	0.0722	0.0506
$\min(h(x,y,20))$	0.0716	0.0944	0.1118	0.0906	0.0471
$\min(h(x,y,25))$	0.0343	0.0454	0.0492	0.0382	0.0268
$\max(c(x,y,5))$	1.1135	1.1069	1.0873	1.2392	1.5629
$\max(c(x,y,10))$	1.3925	1.3132	1.1722	1.5091	2.7505
$\max(c(x,y,15))$	1.6975	1.4593	1.2673	1.9892	5.3456
$\max(c(x,y,20))$	2.4841	1.6448	1.3852	2.6045	5.9684
$\max(c(x,y,25))$	4.8031	1.7733	1.5124	3.1486	6.0538

Table 3: Extreme values for various cases. $P_c(x,y)$ denotes the variable permeability case and is given by Equation (2.3).

Zubkov et al. (2012) studied a system that included both tear film and osmolarity dynamics on a 1D domain with a moving end that mimicked blinks; their model assumes that the ocular surface is impermeable. To compare with their model, we set $P_c = 0$ and show the cross-sectional plots through the vertical line $x = 0$; the results are in Figure 9. The cross-sectional curves of our results on the 2D eye-shaped domain are comparable to the 1D results of Zubkov et al. (2012) during the interblink phase for both the tear film thickness (Figure 9a) and the osmolarity distribution (Figure 9b), except that the development of black line is slower and the maximum osmolarity is higher in our results. The slower development of the black line in our results is due to the stationary domain, because the formation of black line begins during the opening phase according to previous results on 1D blinking domains (Jones et al., 2005; Heryudono et al., 2007; Braun and King-Smith, 2007; Maki et al., 2008; Zubkov et al.,

t= 25   t= 25

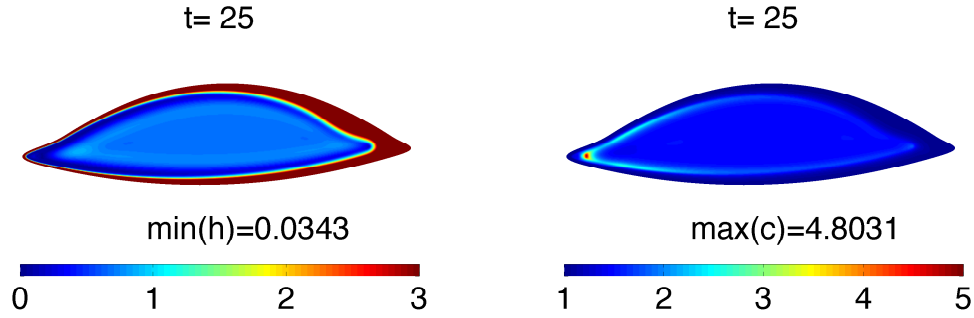min(h)=0.0343   max(c)=4.8031

FIG. 8: Contours of tear film thickness (left) and osmolarity (right) with $P_c = 0$ and Dirichlet boundary condition (2.6). The thinning rate is 4μm/min.

2012). Nevertheless, the behavior of the tear film thickness in our model is in line with many previous results of 1D models with stationary ends (Braun and Fitt, 2003; Winter et al., 2010; Li and Braun, 2012). The difference between the values of osmolarity stemmed from the different assumptions of the thinning rate and our longer time for computing the solution. The thinning rate in the model of Zubkov et al. (2012) is assumed to be 0.24μm/min, which is much smaller than most of the observations of Nichols et al. (2005) and our choice of 4μm/min. Zubkov *et al.* have also considered various evaporation rates to deduce that evaporation increases osmolarity, and they computed results for only 5 seconds, which explains the larger values of osmolarity we obtain as shown in Figure 9b.
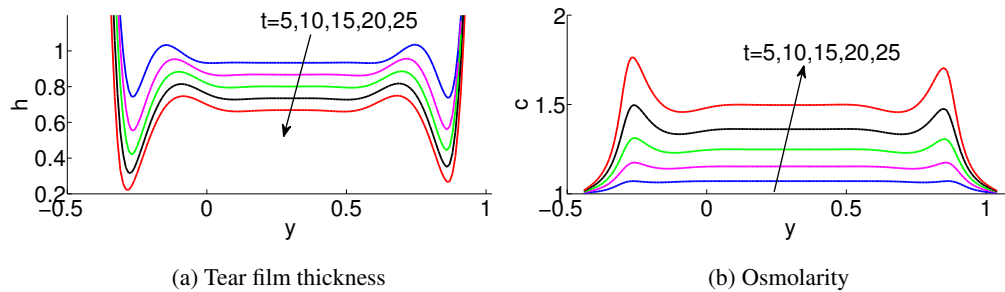

(a) Tear film thickness   (b) Osmolarity

FIG. 9: Cross-sectional plots through the vertical line $x = 0$ with $P_c = 0$ and Dirichlet boundary condition (2.6). The thinning rate is 4μm/min and the upper eyelid is on the positive side of y-axis.

4.3 *Variable Permeability*

In this section, we present simulated results by specifying the variable permeability $P_c(x, y)$ as defined in Equation (2.3). Figure 10 shows time sequences of the contours for both tear film thickness (left column) and osmolarity distribution (right column). Most of the dynamics of tear film thickness
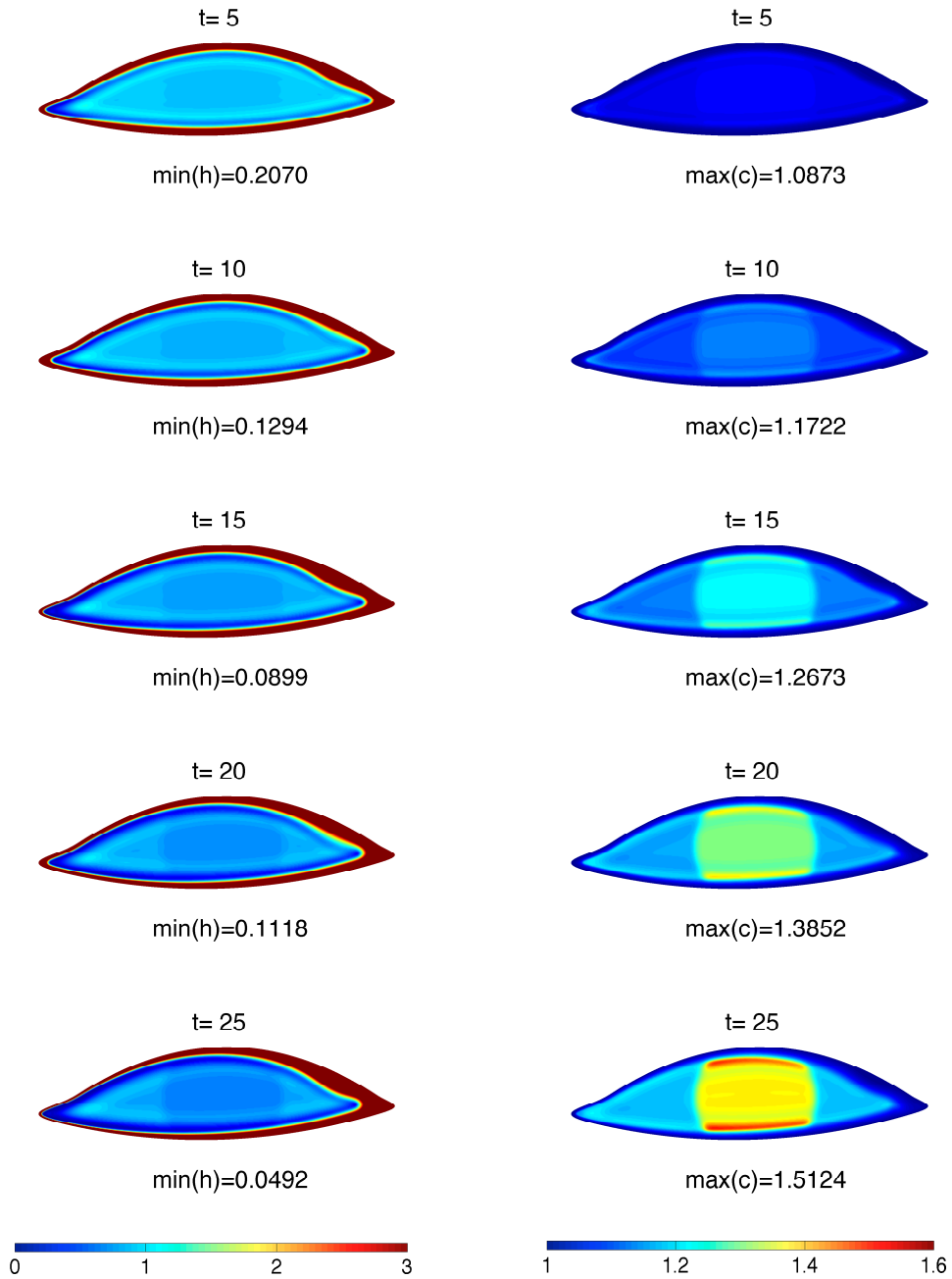
FIG. 10: Contours of tear film thickness (left column) and osmolarity (right column) with variable permeability (2.3) and Dirichlet boundary condition (2.6). The thinning rate is 4μm/min.

are similar to previous cases, such as the development of black line and the continuously thinning in the interior as a result of evaporation. However, due to the variable permeability of the ocular surface, we observe different patterns of tear film thickness over the conjunctival region and the corneal region in the left column of Figure 10. Since the cornea is less permeable, we see in the thickness plots that the tear film is thinner in the corneal region; it appears as a darker (blue) island in the center of the eye-shaped domain.

For the osmolarity distribution shown in the right column of Figure 10, several new patterns are observed beyond the elevated osmolarity in the black line region and the increasing of osmolarity due to evaporation. Because the cornea is less permeable than the conjunctiva, less osmotic flow is expected through the cornea, and this expectation is clearly captured by the model. In the osmolarity contours in Figure 10, we can clearly see a brighter disk in the region of cornea indicating higher osmolarity there. Combining the effect of surface tension and evaporation, the osmolarity is even larger in the black line region over the cornea, and the global maximum of osmolarity is attained there. Comparing with the constant permeability case, both $\min(h)$ and $\max(c)$ are slightly changed since, in the variable permeability case, we have a more permeable conjunctiva.

In order to better observe the transition from conjunctiva to cornea, we plot the horizontal cross-sectional plots (through the line $y = 0.3$ which is roughly across the geometric center of the cornea (GCC)) in Figure 11. Because of the puncta drainage and lacrimal gland supply specified by the time dependent fluid flux boundary condition (2.5), the tear film thickness is much smaller for $x < 0$ in Figure 11a. A local minimum of the tear film thickness, or black line, is still observed in the canthus regions due to the curvature of the menisci. The abrupt change of permeability from conjunctiva to cornea is reflected by the tear film thickness. In Figure 11a, we see a rapid drop of tear film thickness around $x = \pm 1$ near the boundary of cornea. The transition of permeability influences the osmolarity distribution even more dramatically. After $t = 10$, the osmolarity in the cornea surpasses the osmolarity in the nasal canthus (the location of global peak of osmolarity for the zero and constant permeability cases).

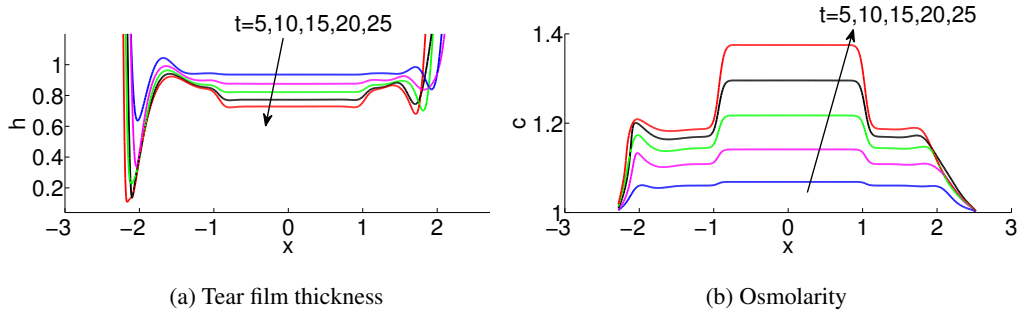(a) Tear film thickness   (b) Osmolarity

FIG. 11: Cross-sectional plots through the horizontal line $y = 0.3$ with variable permeability (2.3) and Dirichlet boundary condition (2.6). Thinning rate is 4μm/min and the temporal canthus is located at the positive side of x-axis.

4.3.1 *Diffusion*   Diffusion also plays a role in the osmolarity dynamics. In Figure 12, we plot the diffusive term, $-[\nabla \cdot (h\nabla c)]/(h\mathrm{Pe}_c)$, in the c equation over the eye-shaped geometry to investigate its

influence on the whole model system. From Figure 12, we see that the diffusion is non-negligible (indicated by the lighter colors and the magnitude is greater than 10^{-2}) inside the black line regions; diffusion is actually of the same size as advection in the black line regions at $t = 20$. Our direct plots of diffusion term on the eye-shaped domain confirmed the results on 1D domain of Zubkov et al. (2012), who studied diffusion by comparing computed results for models with and without diffusivity. Even though the Pèclet number is large in the model system, diffusion helps to ameliorate the high osmolarity level in the black line regions. Diffusion could affect the osmolarity distribution similarly in local spots of break-up (Peng et al., 2014).
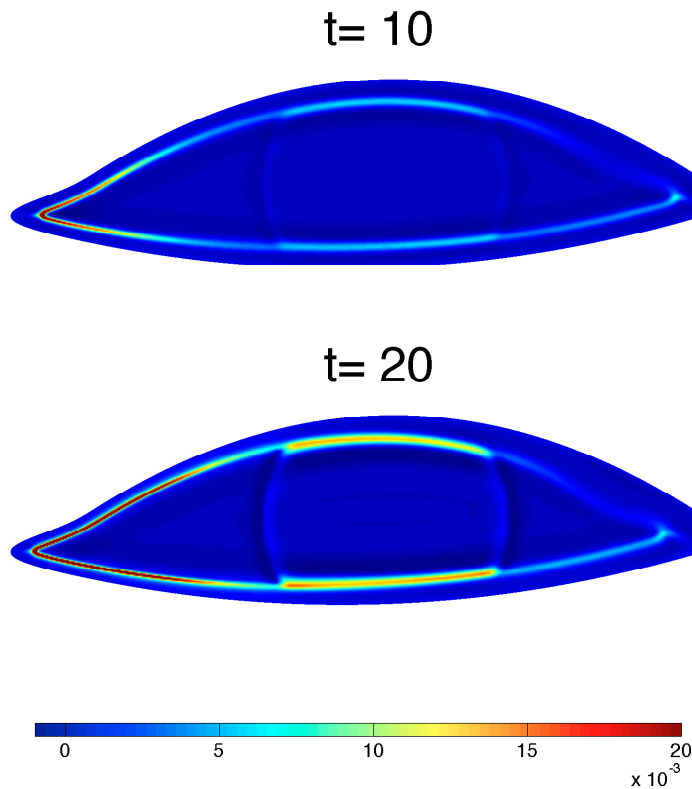

FIG. 12: The contribution of diffusion to osmolarity dynamics. Diffusion is larger (magnitude greater than 10^{-2}) in the lighter areas.

4.3.2 *Movement of Fluid and Solutes*   Figure 13 shows the quiver plots of the fluid flux $\mathbf{Q}$ at time $t = 1$ and $t = 20$. The normalized arrows in the plots show the directions only, and we use the shading to indicate the magnitude of the flux vector: the darker the background, the smaller the flux. In particular

white indicates a flux greater than 10^{-2}; dark gray is less than 10^{-3}. At $t = 1$, the formation of black line dominates the movement of tear fluid. We see from the first plot of Figure 13 that relatively fast flow ($||\mathbf{Q}|| \geqslant 10^{-2}$) is observed near the menisci, and all the arrows pointing towards the eye lids. This is because the lower pressure created by the menisci attracts the nearby fluid forming a locally thin region. This thin region is referred to as the black line and corresponds to the dark blue band as we pointed out in the thickness contour plots previously. In the second plots of Figure 13, relatively fast fluid motion ($||\mathbf{Q}|| \geqslant 10^{-2}$) still occurs in the menisci; however, the arrows in the menisci show that the flow splits near the lacrimal gland and moves towards the nasal canthus along the eye lids. This hydraulic connectivity is thought to be caused by the pressure difference created by the time dependent influx and efflux on the boundary. The pressure gradient in the menisci drives the fluid flows towards the nasal side.

Li et al. (2014) have studied tear flow over the eye-shaped geometry specifying the same time dependent flux BC (2.5). They discovered that, after the development of the black line, relatively fast fluid flow occurs in the menisci corresponding to the experimentally observed hydraulic connectivity, while on the inner side of the black line region, fluid flow is small. The model in this paper couples the fluid dynamics in the tear film with the osmolarity and still captures hydraulic connectivity.

The model equations (2.1) and (2.2) can be combined as a single PDE (Peng et al., 2014):

$$\partial_t (ch) + \nabla \cdot \left(c\mathbf{Q} - \frac{h}{Pe_c} \nabla c \right) = 0. \tag{4.1}$$

Here ch represents the mass per unit area of the solute. From this equation, we see that the solute would move with fluid flow, $\nabla \cdot (c\mathbf{Q})$, and would diffuse from higher concentration to lower concentration $\nabla \cdot (-h\nabla c)/Pe_c$. However, since we have a very large Péclet number for the osmolarity, we expect the solute to move primarily with the fluid flow. Figure 14 shows the contours of the change of the mass per area as opposed to its initial condition: $c(x,y,t)h(x,y,t) - c(x,y,0)h(x,y,0)$. Blue indicates a decrease of mass, while red represents an increase at that location. The left plot of Figure 14 shows the redistribution of the solute at $t = 1$. We see a decrease of mass in the black line region and increase of mass in the menisci corresponding to the formation of black line; it matches with fluid movement as shown in Figure 13. At $t = 20$, the redistribution of mass (right plot of Figure 14) also matches the fluid motion; the increase of solute mass corresponds to the influx from the lacrimal gland, and subsequent flow around the meniscus. The decreases can be explained by the drainage that occurred at the puncta. Another interesting point we note from Figure 14 is that variable permeability does not have an effect on ch, because Equation (4.1) does not depend on permeability at all. In general, solutes in the tear fluid move mostly with the fluid flow. Throughout the time considered, the change of $c(x,y,t)h(x,y,t)$ is rather small in the interior, and thus the reciprocal relation between c and h generally holds in the interior eye.

4.4 *Increased Evaporation Rate*

The average thinning rate for the precorneal tear film (PCTF) measured by Nichols et al. (2005) is $3.79 \pm 4.20\mu$m/min, with the fastest observed PCTF thinning rate being 20μ/min. We attempt to investigate how evaporation influences tear film and osmolarity dynamics by adjusting the parameters

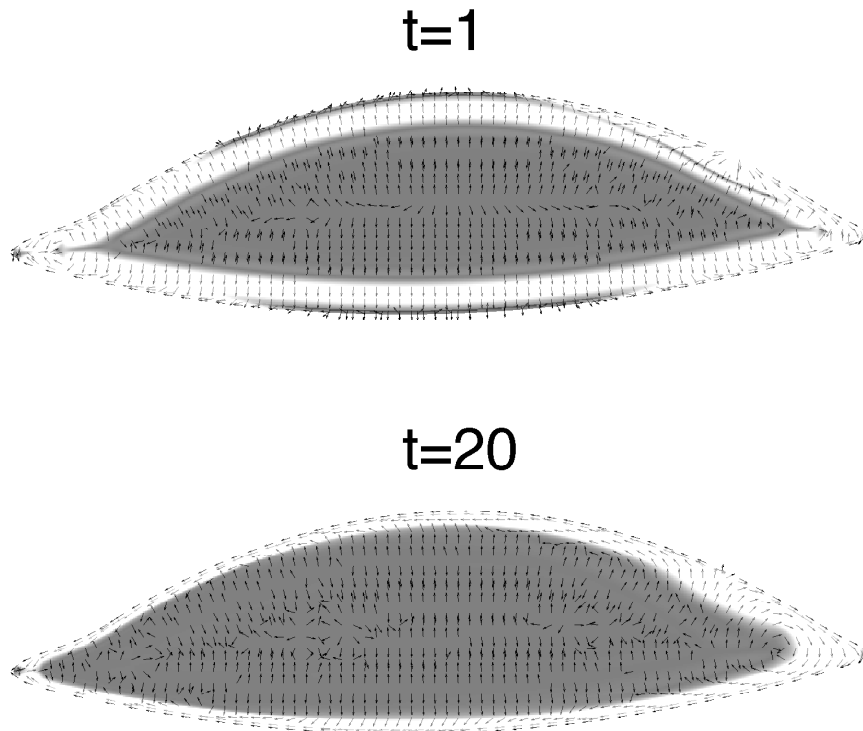FIG. 13: Fluid flux (**Q**) over contours of its magnitude with variable permeability and thinning rate 4μm/min. (Far fewer arrows than the computational grid points are shown for clarity. All the arrows in this plot start at different locations.)

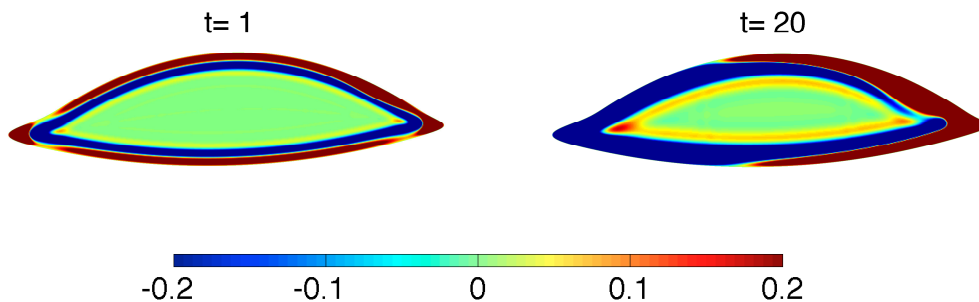FIG. 14: Contour for $c(x,y,t)h(x,y,t) - c(x,y,0)h(x,y,0)$ with variable permeability and thinning rate 4μm/min.

that correspond to an increased thinning rate: 20μm/min.

Figure 15 shows the contours of both $h(x,y,t)$ and $c(x,y,t)$ with parameters specified such that the thinning rate for a flat film is 20μm/min and with variable permeably. Compared with the previous results for the normal thinning rate (4μm/min), we observe the following effects deduced by elevated evaporation. In the thickness contour plots, we observe that the black line forms more rapidly, the interior tear film thickness decreases faster to a thinner level, the global minimum is smaller, and the transition from conjunctiva to cornea is more obvious. The associated osmolarity contours indicate
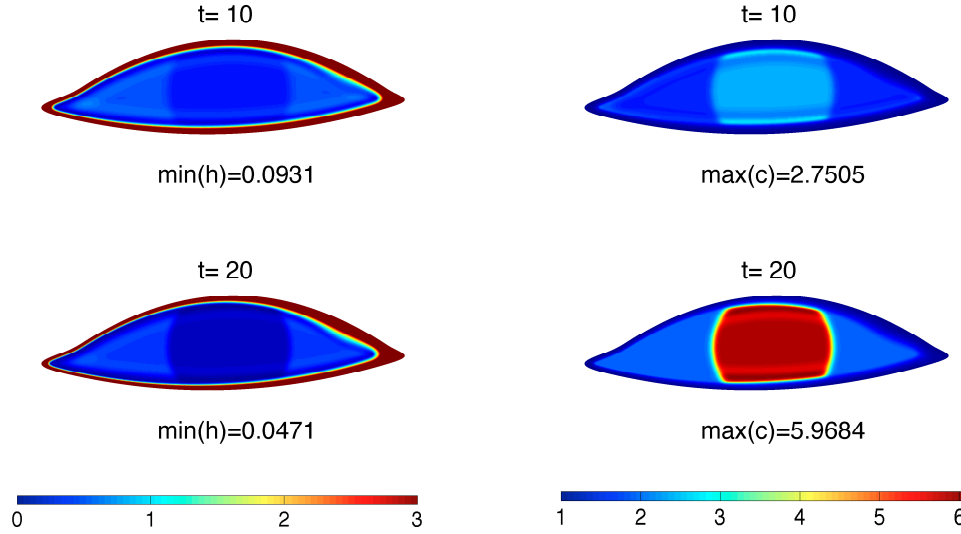
FIG. 15: Contours of tear film thickness (left column) and osmolarity (right column) with variable permeability (2.3) and Dirichlet boundary condition (2.6). The thinning rate is 20μm/min.

the osmolarity is more elevated with a larger global maximum value than the previous 4μm/min case. Moreover, the osmolarity difference between cornea and conjunctiva is more pronounced. In addition, we can see that tear film thins faster with higher evaporation by comparing the extreme values listed in Table 3. We deduce that evaporation increases osmolarity, confirming the 1D results of Zubkov et al. (2012).

The horizontal cross-sectional plots shown in Figure 16 give another view of the tear film thickness and osmolarity, as well as their correlation. Clearly, the tear film becomes much thinner and osmolarity is much more elevated, especially over the corneal region (roughly $-1 \leqslant x \leqslant 1$) than with the normal thinning rate (4μm/min) case (Figure 11). The jump from cornea to conjunctiva is more obvious in both h and c. Higher osmolarity induces a larger osmotic flux from the ocular surface. Even though the thinning rate is 5 times larger, the change in the film thickness and osmolarity are less than a factor of 5 different than those in Figure 11 and Table 3.

4.5 *Osmotic Flux*

A healthy eye is able to maintain a balance between tear loss and supply in a blink cycle. In our model system, we impose time-dependent tear fluid supply and drainage on the boundary that are balanced over a flux cycle ($\Delta t_{bc} = 10$). Over the ocular surface, water leaves the system by evaporation and is supplied by osmotic flux. We now study how the osmotic flux responds to evaporation, and if, at some point, the evaporative loss and osmotic flux reach a dynamic equilibrium over the entire eye.
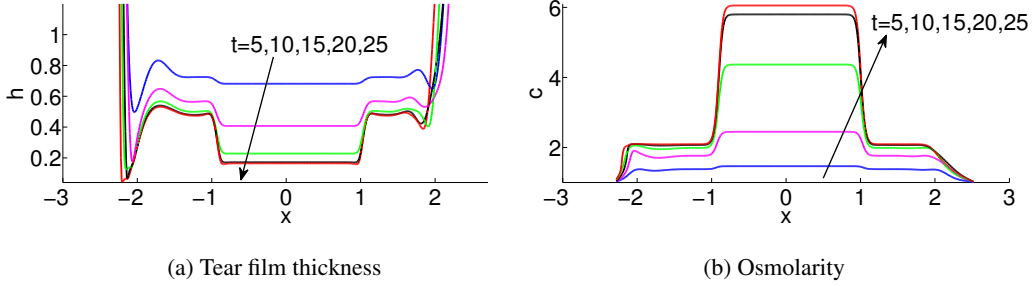
(a) Tear film thickness

(b) Osmolarity

FIG. 16: Cross-sectional plots through the horizontal line $y = 0.3$ with variable permeability (2.3) and Dirichlet boundary condition (2.6). Thinning rate is 20μm/min and the temporal canthus locates at the positive side of x-axis.

(a) Thinning rate is 20μm/min

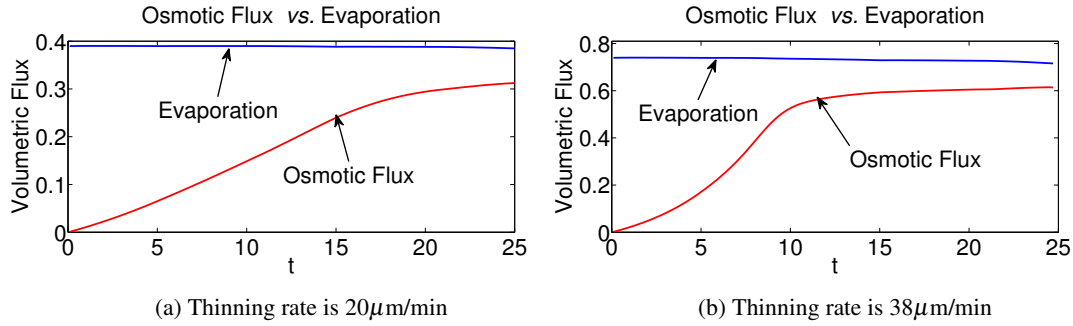(b) Thinning rate is 38μm/min

FIG. 17: Competition between evaporative loss and osmotic flux (volume/time)

To evaluate the volumetric flux of evaporation and osmosis, we integrate the PDE (2.1) over the eye-shaped domain Ω and find:

$$\text{volumetric flux of evaporation: } F_e(t) = \iint_\Omega EJ\,dA,$$

$$\text{volumetric flux of osmosis: } F_o(t) = \iint_\Omega P_c(c-1)\,dA.$$

We plot $F_e(t)$ and $F_o(t)$ together in Figure 17 to investigate the competition between evaporation and osmosis over the eye-shaped domain. Both plots in Figure 17 are simulation results with variable permeability, but with different thinning rates. Note that 38μm/min is the thinning rate of the bare water interface (Peng et al., 2014). As is seen in the plots, osmotic flux is induced immediately in the simulations. The osmotic flux increases much faster with the higher thinning rate (38μm/min), and is seen to reach an equilibrium after $t = 15$. The volumetric flux of evaporation stays almost constant for the 20μm/min case, while a slight decrease is observed for the 38μm/min case. Faster evaporation makes the tear film thin faster, and reach the equilibrium thickness at more locations on the eye. The presence of van der Waals forces prevents the tear film from completely dewetting the ocular surface, and evaporation is shut off when and where a very thin equilibrium h is reached. This results in a decrease of

volumetric flux of evaporation over the entire eye. We believe that ultimately the evaporation and osmosis would balance each other and the system would achieve a dynamic equilibrium. However, we can not verify this because the pressure gradient inside the tear film, between the meniscus and the interior, becomes too steep for our current numerical methods to accurately resolve after $t = 25$. Similar issues limited the amount of time that could be computed in previous models as well (Maki, Braun, Henshaw and King-Smith, 2010; Maki, Braun, Ucciferro, Henshaw and King-Smith, 2010; Li et al., 2014). We also doubt that the equilibrium between evaporation and osmosis can be observed in experiments because, before the equilibrium is reached, reflex tearing and/or blinks are more likely induced when the osmolarity level is high enough.

4.6 *Neumann Boundary Condition for the Osmolarity*

We also consider the homogenous Neumann boundary condition (2.7) for our system. It specifies no flux for osmolarity on the boundary; that is, solute cannot pass through the boundary. The computed results with this Neumann boundary condition (2.7) is rather similar to previous results using the Dirichlet boundary condition (2.6). This is because there is a large amount of fluid in the menisci and the fluid interaction between the menisci and interior is small due to the presence of black line separating them. Our numerical simulations using the Neumann boundary condition (2.7) also confirm that there is negligible difference from the results of using the Dirichlet boundary condition (2.6). Therefore, we don't include the results of the Neumann condition in this paper. However, results of the Neumann boundary condition are used to check the conservation of solute mass in our model system as an indication of numerical accuracy.

We now turn to checking conservation of solute over the domain. Integration of Equation (4.1) over the domain Ω gives the rate of change of the overall solute mass:

$$\partial_t M(t) + \iint_\Omega \nabla \cdot \left(c\mathbf{Q} - \frac{h}{Pe_c} \nabla c \right) dA = 0.$$

Using the divergence theorem we obtain

$$\partial_t M(t) + \oint_{\partial \Omega} \left(c\mathbf{Q} - \frac{h}{Pe_c} \nabla c \right) \cdot \mathbf{n}_b \, dS = 0, \tag{4.2}$$

where $M(t) = \iint_\Omega ch \, dA$ is the total mass of solute over the eye at time t. If we specify zero flux boundary condition for the fluid,

$$\mathbf{Q} \cdot \mathbf{n}_b \Big|_{\partial \Omega} = 0 \tag{4.3}$$

and homogenous Neumann boundary condition (2.7) for the osmolarity, then we conclude from Equation (4.2) that

$$M(t) = M(0),$$

that is, the amount of solute mass is conserved over time. If our numerical simulation is reliable, the difference of mass defined as $\Delta M(t) = |M(t) - M(0)|$, where $M(t)$ is computed numerically, should remain small throughout the simulation, and the magnitude of $\Delta M(t)$ can be regarded as an indication of the performance of the underlying numerical method as described in Section §3.

Table 4 lists both the absolute and relative changes of solute mass at various time for the computation with zero fluid flux BC and homogeneous Neumann BC for the osmolarity. The mass is not exactly

Time	$\Delta M(t)$	Percentage of $M(0)$
5	0.0345	0.2452%
10	0.0542	0.3756%
15	0.0689	0.4774%
20	0.0812	0.5625%
30	0.1012	0.7015%

Table 4: Conservation of mass with boundary conditions (4.3) & (2.7)

conserved because numerical errors are introduced at every time step, and they are accumulated slowly with time. From Table 4, we see that $\Delta M(t)$ increases with time, however, the growth is not exponential, which can be regarded as a numerical evidence that the method is stable. Moreover, the numerical method we use is able to keep $\Delta M(t)$ very small throughout the computation; the relative change of mass is below 1%.

5. Conclusion

The mathematical model in this paper combines tear film flow, evaporation, osmolarity and osmosis on an eye-shaped domain representing the exposed ocular surface. To our knowledge, this is the first such model that includes the osmolarity in a two-dimensional tear film model. The results give information that we believe is not available from human subjects or animal models of the tear film. We believe that these results help give context to osmolarity measurements *in vivo* (Benelli et al., 2010; Lemp et al., 2011, e.g.,). The results show that the location and value of the minimum tear film thickness and maximum osmolarity are found to be sensitive to the permeability at the tear/eye surface.

Measurements of tear film osmolarity in human subjects are made from the inferior meniscus, or more commonly, the temporal canthus. These measurements have been calibrated with respect to DES so that diagnosis of DES is possible with better single-measurement specificity and sensitivity than other single signs or symptoms of DES (Gilbard et al., 1978; Lemp et al., 2011; Sullivan, 2014). But how do those measurements relate to what is going on in the dynamics of the rest of the tear film? For low evaporation rates of 1 micron/min or less, our results are similar to those of Zubkov et al. (2012), with modest increases of osmolarity away from meniscus and particularly in the black line. For larger evaporation rates and longer interblink times, such as those that may be encountered in clinical experiments, our results indicate higher osmolarities. With variable permeability as suggested by experimental measurement (King-Smith et al., 2010), we find that for 4μm/min thinning rates, the peak value of the osmolarity increases 51% over the isotonic value, or about 457 Osm/m^3. This is just at the edge of sensory detection according to the results of Liu et al. (2009), assuming that there is no neuropathy present that would reduce sensory perception at the ocular surface. For 10 and 20 μm/min thinning rates, we obtain maximum values of 951 and 1828 Osm/m^3, respectively; these values are quite high compared to what is mentioned for measurements reported in the literature, and would certainly be felt by subjects with normal neural function (Liu et al., 2009). For all of these cases, the maximum occurs in the black line over the cornea. For the current model, there is very little change in the osmolarity in the outer canthus, which would make it difficult to use that location to deduce the different maxima in the osmolarity.

There are some limitations to the current study for linking the osmolarity measured *in vivo* with the computed results. (i) In our model, there is no lid motion to mix the tear fluid as occurs *in vivo*. This

may be a significant component to the variability observed *in vivo*. (ii) Once the black line is formed in the computed results, there is little exchange between the tear film in the interior with the meniscus. The supply and drainage of tear fluid occurs in and affects primarily the meniscus, and this tends to hold the meniscal values of the osmolarity close to the isotonic value. (iii) The volume of tear fluid is probably large compared to DES subjects, and could affect the values of osmolarity obtained. (iv) The model does not include break up per se, and there have been results that suggest that the osmolarity could be quite high in these localized regions (e.g., Liu et al., 2009; King-Smith et al., 2010; Braun et al., 2010; Braun, 2012; Peng et al., 2014). These points suggest possible fruitful directions for future research. Additional directions would include an dynamic lipid layer that affects the evaporation rate in a sensible way on the eye-shaped domain; possible models are those of of Bruna and Breward (2014) and Peng et al. (2014).

Acknowledgement

References

Amparo, F., Hamrah, P., Schaumberg, D. A. and Dana, R. (2014). The value of tear osmolarity as a metric in evaluating the response to dry eye therapy in the clinic and in clinical trials, *Am. J. Ophthalmol.* **157**: 915–916.

Amparo, F., Jin, Y., Hamrah, P., Schaumberg, D. A. and Dana, R. (2013). What is the value of incorporating tear osmolarity measurement in assessing patient response to therapy in dry eye disease?, *Am. J. Ophthalmol.* **157**: 69–77.e2.

Anonymous (2007). Report of the International Dry Eye WorkShop (DEWS), *Ocul. Surf.* **5**: 65–204.

Baudouin, C., Aragona, P., Messmer, E. M., Tomlinson, A., Calonge, M., Boboridis, K. G., Akova, Y. A., Geerling, G., Labetoulle, M. and Rolando, M. (2013). Role of hyperosmolarity in the pathogenesis and management of dry eye disease: Proceedings of the ocean group meeting, *Ocul. Surf.* **11**: 246–258.

Benelli, U., Nardi, M., Posarelli, C. and Albert, T. G. (2010). Tear osmolarity measurement using the TearLab^{TM} osmolarity system in the assessment of dry eye treatment effectiveness., *Contact Lens Anterior Eye* **33**: 61–67.

Berger, R. E. and Corrsin, S. (1974). A surface tension gradient mechanism for driving the pre-corneal tear film after a blink, *J. Biomech.* **7**: 225–228.

Braun, R. J. (2012). Dynamics of the tear film, *Annu. Rev. Fluid Mech.* **44**: 267–297.

Braun, R. J. and Fitt, A. D. (2003). Modeling the drainage of the precorneal tear film after a blink, *Math. Med. Biol.* **20**: 1–28.

Braun, R. J., Gewecke, N., Begley, C. G., King-Smith, P. E. and Siddique, J. I. (2014). A model for tear film thinning with osmolarity and fluorescein, *Invest. Ophthalmol. Vis. Sci.* **55**: 1133–1142.

Braun, R. J. and King-Smith, P. E. (2007). Model problems for the tear film in a blink cycle: Single equation models, *J. Fluid Mech.* **586**: 465–490.

Braun, R. J., King-Smith, P. E., Nichols, J. J. and Ramamoorthy, P. (2010). On computational models for tear film and osmolarity dynamics, *6th International Conference on the Tear Film and Ocular Surface: Basic Science and Clinical Relevance* **Poster 46**: (abstract).

Braun, R. J., Usha, R., McFadden, G. B., Driscoll, T. A., Cook, L. P. and King-Smith, P. E. (2012). Thin film dynamics on a prolate spheroid with application to the cornea, *J. Eng. Math.* **73**: 121–138.

Brenan, K. E., Campbell, S. L. and Petzold, L. R. (1996). *Numerical Solution of Initial-Value Problems in Differential-Algebraic Equations*, SIAM, Philadelphia.

Bron, A., Tiffany, J., Gouveia, S., Yokoi, N. and Voon, L. (2004). Functional aspects of the tear film lipid layer, *Exp. Eye Res.* **78**: 347–360.

Bruhns, J. L., Braun, R. J., Evans, R. M., Freeman, D. B., King-Smith, P. E., Ramamoorthy, P. and Nichols, J. J. (2014). Models for interaction of the tear film with the corneal and conjunctival epithelia, *(in preparation)* .

Bruna, M. and Breward, C. J. W. (2014). The influence of nonpolar lipids on tear film dynamics, *J. Fluid Mech.* **746**: 565–605.

Chesshire, G. and Henshaw, W. D. (1990). Composite overlapping meshes for the solution of partial differential equations, *J. Comput. Phys.* **90**: 1–64.

Dartt, D. A. (2002). Regulation of mucin and fluid secretion by conjunctival epithelial cells, *Prog. Ret. Eyt Res.* **21**: 555–576.

Deng, Q., Braun, R. J. and Driscoll, T. A. (2014). Heat transfer and tear film dynamics over multiple blink cycles, *Phys. Fluids* **26**: 071901.

Deng, Q., Driscoll, T. A., Braun, R. J. and King-Smith, P. E. (2013). A model for the tear film and ocular surface temperature for partial blinks, *Interfacial Phen. Ht. Trans.* **1**: 357–381.

Doane, M. (1989). An instrument for in vivo tear film interferometry, *Optom. Vis. Sci.* **66**: 383–388.

Doane, M. G. (1981). Blinking and the mechanics of the lacrimal drainage system, *Ophthalmology* **88**: 844–851.

Gilbard, J. P., Farris, R. L. and Santamaria, J. (1978). Osmolarity of tear microvolumes in keratoconjunctivitis sicca, *Arch. Ophthalmol.* **96**: 677–681.

Gipson, I. K. (2004). Distribution of mucins at the ocular surface, *Exp. Eye Res.* **78**: 379–388.

Golding, T. R., Bruce, A. S. and Mainstone, J. C. (1997). Relationship between tear-meniscus parameters and tear-film breakup, *Cornea* **16**: 649–661.

Govindarajan, B. and Gipson, I. (2010). Membrane-tethered mucins have multiple functions on the ocular surface, *Exp. Eye Res.* **90**: 655–693.

Harrison, W. W., Begley, C. G., Liu, H., Chen, M., Garcia, M. and Smith, J. A. (2008). Menisci and fullness of the blink in dry eye, *Optom. Vis. Sci.* **85**: 706–714.

Henshaw, W. D. (2002). Ogen: the overture overlapping grid generator, *Technical Report UCRL-MA-132237*, Lawrence Livermore National Laboratory.

Heryudono, A., Braun, R. J., Driscoll, T. A., Cook, L. P., Maki, K. L. and King-Smith, P. E. (2007). Single-equation models for the tear film in a blink cycle: Realistic lid motion, *Math. Med. Biol.* **24**: 347–377.

Holly, F. (1973). Formation and rupture of the tear film, *Exp. Eye Res.* **15**: 515–525.

Jensen, O. E. and Grotberg, J. B. (1993). The spreading of heat or soluble surfactant along a thin liquid film, *Phys. Fluids A* **75**: 58–68.

Johnson, M. E. and Murphy, P. J. (2004). Changes in the tear film and ocular surface from dry eye syndrome, *Prog. Ret. Eye Res.* **23**: 449–474.

Jones, M. B., McElwain, D. L. S., Fulford, G. R., Collins, M. J. and Roberts, A. P. (2006). The effect of the lipid layer on tear film behavior, *Bull. Math. Biol.* **68**: 1355–1381.

Jones, M. B., Please, C. P., McElwain, D. L. S., Fulford, G. R., Roberts, A. P. and Collins, M. J. (2005). Dynamics of tear film deposition and drainage, *Math. Med. Bio.* **22**: 265–288.

Kimball, S. H., King-Smith, P. E. and Nichols, J. J. (2010). Evidence for the major contribution of evaporation to tear film thinning between blinks, *Invest. Opthalmol. Vis. Sci.* **51**: 6294–6297.

King-Smith, P. E., Fink, B. A., Hill, R. M., Koelling, K. W. and Tiffany, J. M. (2004). The thickness of the tear film, *Curr. Eye. Res.* **29**: 357–368.

King-Smith, P. E., Fink, B. A., Nichols, J. J., Nichols, K. K., Braun, R. J. and McFadden, G. B. (2009). The contribution of lipid layer movement to tear film thinning and breakup, *Invest. Ophthalmol. Visual Sci.* **50**: 2747–2756.

King-Smith, P. E., Nichols, J. J., Nichols, K. K. and Braun, R. J. (2011). A high resolution microscope for imaging the lipid layer of the tear film, *Ocular Surf.* **9**(4): 197–211.

King-Smith, P. E., Nichols, J. J., Nichols, K. K., Fink, B. A., Green-Church, K. B. and Braun, R. J. (2007). Does the water permeability of the corneal surface help prevent excessive evaporative thinning of the tear film?, *5th International Conference on the Tear Film and Ocular Surface: Basic Science and Clinical Relevance*, Taormina, Italy.

King-Smith, P. E., Ramamoorthy, P., Braun, R. J. and Nichols, J. J. (2013). Tear film images and breakup analyzed using fluorescent quenching, *Invest. Ophthalmol. Vis. Sci.* **54**: 6003–6011.

King-Smith, P. E., Ramamoorthy, P., Nichols, K. K., Braun, R. J. and Nichols, J. J. (2010). If tear evaporation is so high, why is tear osmolarity so low?, *6th International Conference on the Tear Film and Ocular Surface: Basic Science and Clinical Relevance* **Poster 43**: (abstract).

Lakowicz, J. R. (2006). *Principal of Fluorescence Spectroscopy*, 3rd edn, Springer, New York.

Lemp, M. A. (2007). The definition and classification of dry eye disease: report of the definition and classification subcommittee of the international dry eye workshop, *Ocul. Surf.* **5**: 75–92.

Lemp, M. A., Bron, A. J., Baudoin, C., Benitez Del Castillo, J. M., Geffen, D., J. Tauber, G. N. F., Pepose, J. S. and Sullivan, B. D. (2011). Tear osmolarity in the diagnosis and management of dry eye disease, *Am. J. Ophthalmol.* **151**: 792–798.

Levin, M. H. and Verkman, A. S. (2004). Aquaporin-dependent water permeation at the mouse ocular surface: In vivo microfluorometric measurements in cornea and conjunctiva, *Invest. Ophthalmol. Vis. Sci.* **45**: 4423–4432.

Li, L. and Braun, R. J. (2012). A model for the human tear film with heating from within the eye, *Phys. Fluids* **24**: 062103.

Li, L., Braun, R. J., Maki, K. L., Henshaw, W. D. and King-Smith, P. E. (2014). Tear film dynamics with evaporation, wetting and time-dependent flux boundary condition on an eye-shaped domain, *Phys. Fluids* **26**: 052101.

Liu, H., Begley, C., Chen, M., Bradley, A., Bonanno, J., McNamara, N. A., Nelson, J. D. and Simpson, T. (2009). A link between tear instability and hyperosmolarity in dry eye, *Invest. Ophthalmol. Vis. Sci.* **50**: 3671–3679.

Maki, K. L., Braun, R. J., Driscoll, T. A. and King-Smith, P. E. (2008). An overset grid method for the study of reflex tearing, *Math. Med. Biol.* **25**: 187–214.

Maki, K. L., Braun, R. J., Henshaw, W. D. and King-Smith, P. E. (2010). Tear film dynamics on an eye-shaped domain I: pressure boundary conditions, *Math. Med. Biol.* **27**: 227–254.

Maki, K. L., Braun, R. J., Ucciferro, P., Henshaw, W. D. and King-Smith, P. E. (2010). Tear film dynamics on an eye-shaped domain. Part 2. Flux boundary conditions, *J. Fluid Mech.* **647**: 361–390.

Mathers, W. and Daley, T. (1996). Tear flow and evaporation in patients with and without dry eye, *Ophthalmol.* **103**: 664–669.

Maurice, D. M. (1973). The dynamics and drainage of tears, *Int. Ophthalmol. Clin.* **13**: 103–116.

McDonald, J. E. and Brubaker, S. (1971). Meniscus-induced thinning of tear films, *Am. J. Ophthalmol.* **72**: 139–146.

Miller, K. L., Polse, K. A. and Radke, C. J. (2002). Black line formation and the "perched" human tear film, *Curr. Eye Res.* **25**: 155–162.

Mishima, S., Gasset, A., Klyce, S. D. and Baum, J. L. (1966). Determination of tear volume and tear flow, *Ophthalmol. Vis. Sci.* **5**: 264–276.

Mishima, S., Kubota, Z. and Farris, R. L. (1971). The tear flow dynamics in normal and in keratoconjunctivitis sicca cases, *in* M. P. Solanes (ed.), *Proceedings of the XXI International Congress, Mexico, DF, 8-14 March, 1970*, Vol. Part 2, pp. 1801–1805.

Mishima, S. and Maurice, D. (1961). The oily layer of the tear film and evaporation from the corneal surface, *Exp. Eye Res.* **1**: 39–45.

Nagyová, B. and Tiffany, J. M. (1999). Components of tears responsible for surface tension, *Curr. Eye Res.* **19**: 4–11.

Nichols, J. J., King-Smith, P. E., Hinel, E. A., Thangavelu, M. and Nichols, K. K. (2012). The use of fluorescent quenching in studying the contribution of evaporation to tear thinning, *Invest. Ophthalmol. Visual Sci.* **53**: 5426–5432.

Nichols, J. J., Mitchell, G. L. and King-Smith, P. E. (2005). Thinning rate of the precorneal and prelens tear films, *Invest. Ophthalmol. Visual Sci.* **46**: 2353–2361.

Norn, M. S. (1979). Semiquantitative interference study of the fatty layer of precorneal film, *Acta Ophthalmol.* **57**: 766–774.

Peng, C.-C., Cerretani, C., Braun, R. J. and Radke, C. J. (2014). Evaporation-driven instability of the precorneal tear film, *Adv. Coll. Interface Sci.* **206**: 250–264.

Pepose, J. S., Sullivan, B. D., Foulks, G. N. and Lemp, M. A. (2014). The value of tear osmolarity as a metric in evaluating the response to dry eye therapy in the clinic and in clinical trials, *Am. J. Ophthalmol.* **157**: 4–6.e1.

Sharma, A., Tiwari, S., Khanna, R. and Tiffany, J. M. (1998). Hydrodynamics of meniscus-induced thinning of the tear film, *in* D. A. Sullivan, D. A. Dartt and M. A. Meneray (eds), *Advances in Experimental Medicine and Biology*, Vol. 438 of *Lacrimal Gland, Tear Film, and Dry Eye Syndromes 2*, Springer, Berlin, pp. 425–431.

Sommeijer, B. P., Shampine, L. F. and Verwer, J. G. (1997). RKC: An explicit solver for parabolic pdes, *J. Comput. Appl. Math.* **88**: 315–326.

Sullivan, B. D. (2014). Challenges in using signs and symptoms to evaluate new biomarkers of dry eye disease, *Ocul. Surf.* **12**: 2–9.

Sullivan, B. D., Whitmer, D., Nichols, K. K., Tomlinson, A., Foulks, G. N., Geerling, G., Pepose, J. S., Kosheleff, V., Porreco, A. and Lemp, M. A. (2010). An objective approach to dry eye disease severity, *Invest. Ophthalmol. Vis. Sci.* **51**: 6125–6130.

TearLab (2013). website, *http://www.tearlab.com* .

Tietz, N. W. (1995). *Clinical Guide to Laboratory Tests*, 3rd edn, W. B. Saunders.

Tiffany, J. M. (1991). The viscosity of human tears, *Int. Ophthalmol.* **15**: 371–376.

Tomlinson, A., Doane, M. G. and McFadyen, A. (2009). Inputs and outputs of the lacrimal system: review of production and evaporative loss, *Ocul. Surf.* **7**: 186–198.

Tomlinson, A., Khanal, S., Ramesh, K. and et al (2006). Tear film osmolarity as a referent for dry eye diagnosis, *Invest. Ophthalmol. Vis. Sci.* **47**: 4309–4315.

Versura, P., Profazio, V. and Campos, E. C. (2010). Performance of tear osmolarity compared to previous diagnostic tests for dry eye diseases, *Curr. Eye Res.* **35**: 553–564.

Wang, J., Fonn, D., Simpson, T. L. and Jones, L. (2003). Precorneal and pre- and postlens tear film thickness measured indirectly with optical coherence tomography, *Invest. Ophthalmol. Vis. Sci.* **44**: 2524–2528.

Webber, W. R. S. and Jones, D. P. (1986). Continuous fluorophotometric method measuring tear turnover rate in humans and analysis of factors affecting accuracy, *Med. Biol. Eng. Comput.* **24**: 386–392.

Winter, K. N., Anderson, D. M. and Braun, R. J. (2010). A model for wetting and evaporation of a post-blink precorneal tear film, *Math. Med. Biol.* **27**: 211–225.

Wong, H., Fatt, I. and Radke, C. J. (1996). Deposition and thinning of the human tear film, *J. Colloid Interface Sci.* **184**: 44–51.

Zhu, H. and Chauhan, A. (2005). A mathematical model for tear drainage through the canaliculi, *Curr. Eye. Res.* **30**: 621–630.

Zubkov, V. S., Breward, C. J. and Gaffney, E. A. (2012). Coupling fluid and solute dynamics within the ocular surface tear film: a modelling study of black line osmolarity, *Bull. Math. Biol.* **74**: 2062–2093.

Appendix

A. Model Derivation

We show detailed derivation of the model system (2.1) & (2.2) below. Inside the tear fluid, we model the tear film fluid with the incompressible Navier-Stokes equations and energy conservation equation, and model the osmolarity dynamics with convection-diffusion equation. Namely, in $0 < z' < h'(x', y', t')$:

$$\rho \left(\partial_{t'} \mathbf{u}' + \mathbf{u}' \cdot \nabla \mathbf{u}' \right) = -\nabla p' + \mu \Delta \mathbf{u}' - \rho g \mathbf{j}, \qquad \rho c_p (\partial_{t'} T' + \mathbf{u}' \cdot \nabla T') = k \Delta T',$$

$$\nabla \cdot \mathbf{u}' = 0, \qquad \partial_t c' + \nabla \cdot \left(c' \mathbf{u}' \right) = D_c \Delta c'.$$

Here c' is the volumetric concentration of osmotically active physiological salts in the aqueous layer. It is measured in units of Osmoles per m^3. D_c is the diffusion coefficient of osmolarity. $(\mathbf{i}, \mathbf{j}, \mathbf{k})$ are the standard basis vectors.

At the free surface, $z' = h'$, we have the equations to balance fluid mass and energy:

$$J' = \rho (\mathbf{u}' - \mathbf{u}'_I) \cdot \mathbf{n}', \qquad L_m J' + k \mathbf{n}' \cdot \nabla T' = 0.$$

Here $\mathbf{u}'_I = \partial_t' h' \mathbf{k}$ is the interfacial velocity and $\mathbf{n}'$ is the normal vector to the tear film surface. The jump of the velocity at the free surface is due to evaporation. We also assume tangential immobility and we balance normal stress with the conjoining pressure under consideration:

$$\mathbf{u}' \cdot \mathbf{t}'_1 = \mathbf{u}' \cdot \mathbf{t}'_2 = 0, \qquad -p'_v - \mathbf{n}' \cdot \mathbf{T}' \cdot \mathbf{n}' = \sigma \nabla \cdot \mathbf{n}' - \Pi'.$$

Here $\mathbf{t}'_1$ and $\mathbf{t}'_2$ are a pair of orthogonal tangential vectors of the tear film surface, $\mathbf{T}' = -p' \mathbf{I} + \mu (\nabla \mathbf{u}' + \nabla \mathbf{u}'^T)$ is the Newtonian stress tensor, and $\Pi' = A^*/h'^3$ is the conjoining pressure. Finally, we relate the interfacial temperature to the mass flux and pressure jump by the nonequilibrium condition, and we impose a no-flux condition for the osmolarity,

$$KJ' = \alpha(p' - p'_v) + T' - T'_s, \qquad (\mathbf{u}' - \mathbf{u}'_I)c' \cdot \mathbf{n}' = D_c \nabla c' \cdot \mathbf{n}'.$$

Since we model the evaporative mass flux J' as

$$J' = \rho (\mathbf{u}' - \mathbf{u}'_I) \cdot \mathbf{n}',$$

the no-flux condition for osmolarity at the free surface becomes

$$D_c \nabla c' \cdot \mathbf{n}' = \frac{c' J'}{\rho}.$$

At the cornea-tear film interface, $z' = 0'$, in addition to the specification of no-slip conditions and the prescription of body temperature, we allow water to go through the ocular surface by osmosis, but keep the physiological salt from penetrating the ocular surface, thus we have

$$u' = v' = 0, \quad T' = T'_B, \quad w' = P'_c(c' - c'_0), \quad w'c' = D_c \partial'_z c'.$$

Here $c'_0 = 302$ Osm/m^3 is the isotonic physiological salt concentration, which is also used to scale c'.

The following scales are used to non-dimensionalize the equations:

$$x' = L'x, \; y' = L'y, \; z' = d'z, \; h' = d'h, \; c' = c'_0\bar{c}, \; u' = U_0 u, \; v' = U_0 v, \; t' = \frac{L'}{U_0}t,$$

$$w' = \frac{d'U_0}{L'}w, \; p' = \frac{\mu U_0}{L'\varepsilon^2}p, \; T = \frac{T' - T'_s}{T'_B - T'_s}, \; J' = \frac{k}{d'\mathscr{L}_m}(T'_B - T'_s)J.$$

Here $\varepsilon = d'/L' \ll 1$ indicates the separation of length scales. After non-dimensionalization, we have, in $0 < z < h(x,y,t)$,

$$\varepsilon^2 \text{Re}\left(\partial_t u + u\partial_x u + v\partial_y u + w\partial_z u\right) = -\partial_x p + \left(\varepsilon^2 \partial_x^2 u + \varepsilon^2 \partial_y^2 u + \partial_z^2 u\right),$$

$$\varepsilon^2 \text{Re}\left(\partial_t v + u\partial_x v + v\partial_y v + w\partial_z v\right) = -\partial_y p + \left(\varepsilon^2 \partial_x^2 v + \varepsilon^2 \partial_y^2 v + \partial_z^2 v\right) - G,$$

$$\varepsilon^4 \text{Re}\left(\partial_t w + u\partial_x w + v\partial_y w + w\partial_z w\right) = -\partial_z p + \varepsilon^2 \left(\varepsilon^2 \partial_x^2 w + \varepsilon^2 \partial_y^2 w + \partial_z^2 w\right),$$

$$\varepsilon^2 \text{RePr}\left(\partial_t T + u\partial_x T + v\partial_y T + w\partial_z T\right) = \varepsilon^2 \left(\partial_x^2 T + \partial_y^2 T\right) + \partial_z^2 T,$$

$$\partial_x u + \partial_y v + \partial_z w = 0,$$

$$\varepsilon^2 \text{Pe}_c \left[\partial_t \bar{c} + (u\partial_x \bar{c} + v\partial_y \bar{c} + w\partial_z \bar{c})\right] = \varepsilon^2 \partial_x^2 \bar{c} + \varepsilon^2 \partial_y^2 \bar{c} + \partial_z^2 \bar{c},$$

at $z = h(x,y,t)$,

$$EJ = \frac{-u\partial_x h - v\partial_y h + w - \partial_t h}{\sqrt{1 + \varepsilon^2 \left(\partial_x h\right)^2 + \varepsilon^2 \left(\partial_y h\right)^2}},$$

$$J + \frac{-\varepsilon^2 \partial_x h \partial_x T - \varepsilon^2 \partial_y h \partial_y T + \partial_z T}{\sqrt{1 + \varepsilon^2 \left(\partial_x h\right)^2 + \varepsilon^2 \left(\partial_y h\right)^2}} = 0,$$

$$\frac{v + \varepsilon^2 w\partial_y h}{\sqrt{1 + \varepsilon^2 \left(\partial_y h\right)^2}} = \frac{u + \varepsilon^2 w\partial_x h}{\sqrt{1 + \varepsilon^2 \left(\partial_x h\right)^2}} = 0,$$

$$p - p_v - \frac{2\varepsilon^2 \left[\varepsilon^2 \left(\partial_x^2 h \partial_x u + \partial_y^2 h \partial_y v + \partial_x h \partial_y h (\partial_y u + \partial_x v) - \partial_x h \partial_x w - \partial_y h \partial_y w\right) + \partial_z w - \partial_x h \partial_z u - \partial_y h \partial_z v\right]}{\sqrt{1 + \varepsilon^2 \left(\partial_x h\right)^2 + \varepsilon^2 \left(\partial_y h\right)^2}}$$

$$= -S \left[\partial_x \left(\frac{\partial_x h}{\sqrt{1 + \varepsilon^2 \left(\partial_x h\right)^2 + \varepsilon^2 \left(\partial_y h\right)^2}}\right) + \partial_y \left(\frac{\partial_y h}{\sqrt{1 + \varepsilon^2 \left(\partial_x h\right)^2 + \varepsilon^2 \left(\partial_y h\right)^2}}\right)\right] - \frac{A}{h^3},$$

$$\bar{K}J = \delta \left(p - p_v\right) + T,$$

$$-\varepsilon^2 \partial_x h \partial_x \bar{c} - \varepsilon^2 \partial_y h \partial_y \bar{c} + \partial_z \bar{c} = E \mathrm{Pe}_c \varepsilon^2 \bar{c} J \sqrt{1 + \varepsilon^2 \left(\partial_x h\right)^2 + \varepsilon^2 \left(\partial_y h\right)^2},$$

at $z = 0$,

$$u = v = 0, \quad T = 1,$$
$$w = P_c(\bar{c} - 1),$$
$$\varepsilon^2 \mathrm{Pe}_c w \bar{c} = \partial_z \bar{c}.$$

$\mathrm{Pe}_c = \dfrac{U_0 L'}{D_c}$ is the Pèclet number for salt and $P_c = \dfrac{P^{\mathrm{tiss}} v_w c_0'}{\varepsilon U_0}$ is the nondimensional permeability of the ocular surface. The tissue permeability P^{tiss} will take on different values as described in Section 2.2.

We estimate the size of the non-dimensional parameters:

$$\varepsilon = \frac{d'}{L'} = 1 \times 10^{-3}, \quad \mathrm{Re} = \frac{U_0 L'}{\mu/\rho} \approx 19.23, \quad \mathrm{Pr} = \frac{c_p \mu}{k} \approx 8.01,$$

where Re is the Reynolds number and Pr is the Prandtl number. Terms involving the following parameters are regarded as small:

$$\varepsilon^2 = 1 \times 10^{-6}, \quad \varepsilon^2 \mathrm{Re} \approx 1.92 \times 10^{-5}, \quad \varepsilon^2 \mathrm{RePr} \approx 1.54 \times 10^{-4}.$$

Applying lubrication theory by neglecting all the small terms for the fluid equations, we then have the following leading order approximations.

In $0 < z < h(x, y, t)$:

$$0 = -\partial_x p + \partial_z^2 u, \tag{A.1}$$
$$0 = -\partial_y p + \partial_z^2 v - G, \tag{A.2}$$
$$0 = -\partial_z p, \tag{A.3}$$
$$0 = \partial_z^2 T, \tag{A.4}$$
$$\partial_x u + \partial_y v + \partial_z w = 0. \tag{A.5}$$

For the osmolarity, we expand $\bar{c}(x, y, z, t)$ as

$$\bar{c} = \bar{c}_0 + \varepsilon^2 \bar{c}_1 + O(\varepsilon^4).$$

So the leading order equation is

$$\partial_z \bar{c}_0 = 0, \tag{A.6}$$

which implies $\bar{c}_0$ is independent of z, i.e. $\bar{c}_0 = \bar{c}_0(x,y,t)$. We proceed to the next order so as to find an equation for $\bar{c}_0$, and we obtain

$$\partial_z^2 \bar{c}_1 = \mathrm{Pe}_c \left[\partial_t \bar{c}_0 + (u\partial_x \bar{c}_0 + v\partial_y \bar{c}_0) \right] - \partial_x^2 \bar{c}_0 - \partial_y^2 \bar{c}_0. \tag{A.7}$$

At $z = h(x,y,t)$:

$$EJ = -u\partial_x h - v\partial_y h + w - \partial_t h, \tag{A.8}$$

$$J + \partial_z T = 0, \tag{A.9}$$

$$u = v = 0, \tag{A.10}$$

$$p - p_v = -S \left(\partial_x^2 h + \partial_y^2 h \right) - \frac{A}{h^3}, \tag{A.11}$$

$$\bar{K}J = \delta (p - p_v) + T, \tag{A.12}$$

$$\partial_z \bar{c}_1 = E\mathrm{Pe}_c \bar{c}_0 J + \nabla h \cdot \nabla \bar{c}_0. \tag{A.13}$$

We use $\nabla = (\partial_x, \partial_y)$ and $\Delta = (\partial_x^2 + \partial_y^2)$ to represent the differential operators applied on them for convenience since both h and $\bar{c}_0$ are independent on z.

At $z = 0$:

$$u = v = 0, \ \ T = 1, \tag{A.14}$$

$$w = P_c(\bar{c}_0 - 1), \tag{A.15}$$

$$\partial_z \bar{c}_1 = \mathrm{Pe}_c P_c(\bar{c}_0 - 1)\bar{c}_0. \tag{A.16}$$

For the tear film, we solve for the velocity and temperature fields, integrate the mass conservation equation and use the kinematic condition to derive a PDE for $h(x,y,t)$:

$$\partial_t h + EJ + \nabla \cdot \mathbf{Q} - P_c(\bar{c}_0 - 1) = 0,$$

with

$$J = \frac{1 - \delta \left(S\Delta h + Ah^{-3} \right)}{\bar{K} + h} \ \ \text{and} \ \ \mathbf{Q} = \left(\int_0^h u \, dz, \int_0^h v \, dz \right) = \frac{h^3}{12} \nabla \left(S\Delta h + Ah^{-3} - Gy \right).$$

For the osmolarity, we integrate Equation (A.7) with respect to z from 0 to h. Noting that $\bar{c}_0 = \bar{c}_0(x,y,t)$, we then have

$$\partial_z \bar{c}_1(x,y,h,t) - \partial_z \bar{c}_1(x,y,0,t) = \mathrm{Pe}_c \left[h\partial_t \bar{c}_0 + \nabla \bar{c}_0 \cdot \mathbf{Q} \right] - h\Delta \bar{c}_0.$$

According to the boundary conditions (A.13) and (A.16), we derive a PDE for $\bar{c}_0(x,y,t)$:

$$\mathrm{Pe}_c \left[h\partial_t \bar{c}_0 + \nabla \bar{c}_0 \cdot \mathbf{Q} \right] - h\Delta \bar{c}_0 = E\mathrm{Pe}_c \bar{c}_0 J + \nabla h \cdot \nabla \bar{c}_0 - \mathrm{Pe}_c P_c(\bar{c}_0 - 1)\bar{c}_0.$$

For convenience, we use c in the equations instead of $\bar{c}_0$. Therefore, we have derived the governing equations (2.1) and (2.2):

$$\partial_t h + EJ + \nabla \cdot \mathbf{Q} - P_c(c - 1) = 0,$$

$$h\partial_t c + \nabla c \cdot \mathbf{Q} = EcJ + \frac{1}{\mathrm{Pe}_c} \nabla \cdot (h\nabla c) - P_c(c - 1)c.$$

B. Time-dependent Fluid Flux Boundary Condition

We define

$$Q_{lg}(s,t) = f_{lg}(t)\hat{Q}_{ls}(s), \quad Q_p(s,t) = f_p(t)\hat{Q}_p(s)$$

in the time-dependent fluid flux BC (2.5). The formulations of $f_{lg}(t), f_p(t), \hat{Q}_{lg}(s)$, and $\hat{Q}_p(s)$ are listed below:

$$f_{lg}(t) = \begin{cases} \frac{1}{2}\left[\cos\left(\frac{\pi}{2}\frac{t-t_{lg,on}}{\Delta t_{lg}} - \frac{\pi}{2}\right) + 1\right], & \text{if } |t-t_{lg,on}| \leqslant \Delta t_{lg}; \\ 1, & \text{if } t_{lg,on} + \Delta t_{lg} \leqslant t \leqslant t_{lg,off} - \Delta t_{lg}; \\ \frac{1}{2}\left[\cos\left(\frac{\pi}{2}\frac{t-t_{lg,off}}{\Delta t_{lg}} + \frac{\pi}{2}\right) + 1\right], & \text{if } |t-t_{lg,off}| \leqslant \Delta t_{lg}; \\ 0, & \text{otherwise}. \end{cases} \tag{B.1}$$

$$f_p(t) = \begin{cases} \frac{1}{2}\left[\cos\left(\frac{\pi}{2}\frac{t-t_{p,on}}{\Delta t_p} - \frac{\pi}{2}\right) + 1\right], & \text{if } |t-t_{p,on}| \leqslant \Delta t_p; \\ 1, & \text{if } t_{p,on} + \Delta t_p \leqslant t \leqslant t_{p,off} - \Delta t_p; \\ \frac{1}{2}\left[\cos\left(\frac{\pi}{2}\frac{t-t_{p,off}}{\Delta t_p} + \frac{\pi}{2}\right) + 1\right], & \text{if } |t-t_{p,off}| \leqslant \Delta t_p; \\ 0, & \text{otherwise}. \end{cases} \tag{B.2}$$

$$\hat{Q}_{lg}(s) = \begin{cases} 0, & \text{if } s < s_{lg,on} - \Delta s_{lg}; \\ -\frac{1}{2}\hat{Q}_{0lg}\left[\cos\left(\frac{\pi}{2}\frac{s-s_{lg,on}}{\Delta s_{lg}} - \frac{\pi}{2}\right) + 1\right], & \text{if } |s-s_{lg,on}| \leqslant \Delta s_{lg}; \\ -\hat{Q}_{0lg}, & \text{if } s_{lg,on} + \Delta s_{lg} \leqslant s \leqslant s_{lg,off} - \Delta s_{lg}; \\ -\frac{1}{2}\hat{Q}_{0lg}\left[\cos\left(\frac{\pi}{2}\frac{s-s_{lg,off}}{\Delta s_{lg}} + \frac{\pi}{2}\right) + 1\right], & \text{if } |s-s_{lg,off}| \leqslant \Delta s_{lg}; \\ 0, & \text{otherwise}. \end{cases} \tag{B.3}$$

$$\hat{Q}_p(s) = \begin{cases} 0, & \text{if } s < s_{p,lo} - \Delta s_p; \\ -\frac{\hat{Q}_{0p}}{2}(1-p_{out})\left[\cos\left(\pi\frac{s-s_{p,lo}}{\Delta s_p} - \pi\right) - 1\right], & \text{if } |s-s_{p,lo}| \leqslant \Delta s_p; \\ 0, & \text{if } s_{p,lo} + \Delta s_p \leqslant s \leqslant s_{p,up} - \Delta s_p; \\ -\frac{\hat{Q}_{0p}}{2}(p_{out})\left[\cos\left(\pi\frac{s-s_{p,up}}{\Delta s_p} - \pi\right) - 1\right], & \text{if } |s-s_{p,up}| \leqslant \Delta s_p; \\ 0, & \text{otherwise}. \end{cases} \tag{B.4}$$

Parameters in the formulations are tabulated in Table 5.

Table 5: Parameters appearing in the flux boundary condition.

Parameter	Description	Value
$t_{lg,on}$	On time for lacrimal gland supply	0.2
$t_{lg,off}$	Off time for lacrimal gland supply	5.2
Δt_{lg}	Transition time of lacrimal gland supply	0.2
$t_{p,on}$	On time for punctal drainage	1.05
$t_{p,off}$	Off time for punctal drainage	5.05
Δt_p	Transition time of punctal drainage	0.05
Q_{mT}	Estimated steady supply from lacrimal gland	0.08
$\hat{Q}_{0lg}$	Height of lacrimal gland peak	0.4
$\hat{Q}_{0p}$	Height of punctal drainage peak	4
Δt_{bc}	Flux cycle time	10
$s_{lg,on}$	On-ramp location for lacrimal gland peak	4.2
$s_{lg,off}$	Off-ramp location for lacrimal gland peak	4.6
Δs_{lg}	On-ramp and off-ramp width of lacrimal peak	0.2
p_{out}	Fraction of drainage from upper punctum	0.5
$s_{p,lo}$	Lower punctal drainage peak location	11.16
$s_{p,up}$	Upper punctal drainage peak location	11.76
Δs_p	Punctal drainage peak width	0.05